NEUROPROSTHETIC BAROREFLEX CONTROLS HEMODYNAMICS AFTER SPINAL CORD INJURY

Jordan W. Squair[1-6], Matthieu Gautier[1]*, Lois Mahe[1]*, Jan Elaine Soriano[4]*, Andreas Rowald[1]*, Arnaud Bichat[1], Newton Cho[1,9], Mark A. Anderson[1], Nicholas D. James[1], Jerome Gandar[1], Anthony V. Incognito[10], Giuseppe Schiavone[11], Zoe K. Sarafis[1], Achilleas Laskaratos[1], Kay Bartholdi[1], Robin Demesmaeker[1,7], Salif Komi[1,7], Charlotte Moerman[7], Bita Vaseghi[4], Berkeley Scott[4], Ryan Rosentreter[4], Claudia Kathe[1], Jimmy Ravier[1], Laura McCracken[1], Xiaoyang Kang[11], Nicolas Vachicouras[11], Florian Fallegger[11], Ileana Jelescu[12], YunLong Cheng[13], Qin Li[13], Rik Buschman[14], Nicolas Buse[14], Tim Denison[15], Sean Dukelow[4], Rebecca Charbonneau[4], Ian Rigby[4], Steven K. Boyd[16], Philip J. Millar[10], Eduardo Martin Moraud[7], Marco Capogrosso[8], Fabien B. Wagner[1,7,17], Quentin Barraud[1], Erwan Bezard[13,17,18], Stéphanie P. Lacour[11], Jocelyne Bloch[1,2,3,7], Grégoire Courtine[1,2,3,7,#] and Aaron A. Phillips[4,6#]

1. Center for Neuroprosthetics and Brain Mind Institute, School of Life Sciences, Swiss Federal Institute of Technology (EPFL), Lausanne, Switzerland
2. Department of Neurosurgery, Lausanne University Hospital (CHUV) and University of Lausanne (UNIL), Lausanne, Switzerland
3. Defitech Center for Interventional Neurotherapies, NeuroRestore, Switzerland
4. Department of Physiology and Pharmacology, Clinical Neurosciences, Cardiac Sciences, Hotchkiss Brain Institute, Libin Cardiovascular Institute of Alberta, Cumming School of Medicine, University of Calgary,
5. MD/PhD Training Program, Faculty of Medicine, University of British Columbia, Vancouver, Canada
6. International collaboration on repair discoveries (ICORD), University of British Columbia, Vancouver, Canada
7. Department of Clinical Neuroscience, Lausanne University Hospital (CHUV) and University of Lausanne (UNIL), Lausanne, Switzerland
8. Faculty of Biology, University of Fribourg, Fribourg, Switzerland
9. Department of Neurosurgery, University of Toronto, Toronto, Canada
10. Department of Human Health and Nutritional Sciences, University of Guelph, Guelph, Canada
11. Centre for Neuroprosthetics, Institute of Microengineering, Swiss Federal Institute of Technology (EPFL), Lausanne, Switzerland
12. Center for Biomedical Imaging, Swiss Federal Institute of Technology (EPFL), Lausanne, Switzerland
13. Motac Neuroscience Ltd, Manchester, United Kingdom
14. Medtronic, Minneapolis, USA
15. Oxford University, Oxford, England
16. Department of Radiology, McCaig Institute for Bone and Joint Health, University of Calgary
17. Université de Bordeaux, Institut des Maladies Neurodégénératives, UMR 5293, F-33000 Bordeaux, France
18. CNRS, Institut des Maladies Neurodégénératives, UMR 5293, F-33000 Bordeaux, France

*, # contributed equally to this work

Corresponding authors:

Grégoire Courtine, PhD
gregoire.courtine@epfl.ch

Aaron A. Phillips, PhD
aaron.phillips@ucalgary.ca

Spinal cord injury (SCI) induces hemodynamic instability that threatens survival[1–3], impairs neurological recovery[4,5], increases cardiovascular disease risk[6,7], and reduces quality of life[8,9]. Hemodynamic instability in this context is due to the interruption of supraspinal efferent commands to sympathetic circuits located in the spinal cord[10], which prevents the natural baroreflex from controlling these circuits to adjust peripheral vascular resistance. We previously showed that epidural electrical stimulation (EES) of the spinal cord can compensate for interrupted supraspinal commands to motor circuits below injury[11], which restored walking after paralysis[12]. Here, we leveraged these concepts to develop EES protocols that restored hemodynamic stability after SCI. We established a novel preclinical model that enabled us to dissect the topology and dynamics of the sympathetic circuits, and understand how EES can engage these circuits. We incorporated these spatial and temporal features into stimulation protocols to conceive a clinical-grade biomimetic hemodynamic regulator operating in closed-loop. This *neuroprosthetic baroreflex* controlled hemodynamics for extended periods of time in rodents, non-human primates, and humans, both after acute and chronic SCI. We will now conduct clinical trials to turn the *neuroprosthetic baroreflex* into a commonly available therapy for people with SCI.

An SCI immediately impairs hemodynamic stability, leading to repeated hypotensive episodes that are life threatening and reduce neurological recovery[1,4,5,13,14]. Daily hypotensive episodes augment the risk of stroke and heart disease[6,7,15], and reduce engagement in social and professional activities[8,9].

This hemodynamic instability is due to the interruption of supraspinal drive to the sympathetic circuitry. Consequently, this circuitry no longer receives efferent commands from brainstem vasomotor regulatory centers, preventing the natural baroreflex from exerting precise control over the sympathetic circuitry that adjusts peripheral vascular resistance[16,17]. EES can compensate for missing regulatory commands from the brain after a SCI[12,18–20]. For example, the delivery of EES with a spatial and temporal sequence that coincides with the ongoing movement reinstated the natural dynamics of motoneuron activation, which restored locomotion after SCI[11,12,21]. Serendipitous observations showed that EES applied over lumbosacral segments can also transiently elevate blood pressure[22-25]. However, lumbosacral segments contain a paucity of sympathetic efferent neurons, casting doubt that this approach harnesses the full potential of EES to activate sympathetic circuits and achieve hemodynamic stability after SCI.

Here, we uncovered the key mechanisms through which EES modulates blood pressure, and leveraged this understanding to conceive a neuroprosthetic baroreflex that precisely controlled hemodynamics over extended periods of time in rodents, non-human primates, and humans – effective from a few hours after SCI to the chronic phase of the condition.

Preclinical model of hemodynamic instability

Rats received a severe clinically-relevant contusion onto thoracic (T3) segments (**Fig. 1a** and **Extended Data Fig. 1**). To visualize how this contusion damaged the descending pathways regulating hemodynamics, we targeted catecholaminergic neurons expressing tyrosine

hydroxylase (TH) by stereotaxic infusions of AAV-DJ-hSyn-flex-mGFP-2A-Synaptophysin-mRuby[26] into the rostral ventrolateral medulla (RVLM) of TH-Cre rats[27]. CLARITY-optimized light-sheet microscopy[28] of TH^{ON} fibers and synapses revealed a near complete depletion of sympatho-excitatory synapses onto ChAT^{ON} sympathetic preganglionic neurons below the injury (**Fig. 1a**).

To characterize the natural history of hemodynamic instability following SCI, we implanted rats with a wireless system that enabled 24/7 monitoring of arterial blood pressure and sympathetic nerve activity (**Fig. 1b** and **Extended Data Fig. 1d-f**). The SCI instantly induced a transient spike in blood pressure and sympathetic nerve activity (**Extended Data Fig. 2b-c**), followed by a pronounced depression that persisted throughout the chronic phase (**Fig. 1d**). 24/7 monitoring of blood pressure and sympathetic nerve activity in home cage revealed that the SCI led to profound hemodynamic instability (**Extended Data Fig. 2d-g**).

Despite the elimination of the sympathetic-vasomotor division of the natural baroreflex, the rats did not exhibit the hypotension observed in humans in response to orthostatic challenges (**Extended Data Fig. 1a**), thus preventing the investigation of this specific physiological mechanism in preclinical models.

To enable such investigations, we developed a servo-controlled negative pressure chamber that mimics orthostatic challenge paradigms used in humans to quantify hemodynamic instability (**Fig. 1c**). Uninjured rats exposed to negative pressure exhibited transient hypotensive episodes. After SCI, rats could no longer recover from the simulated orthostatic challenge (**Fig. 1d**). They exhibited sustained hypotension, the severity of which linearly correlated with the pressure in the chamber (**Extended Data Fig. 2i**).

These results indicate that our preclinical model reproduced the hallmarks of hemodynamic instability observed in humans, and thus established heuristic conditions to dissect the mechanisms through which EES could regulate hemodynamics after SCI.
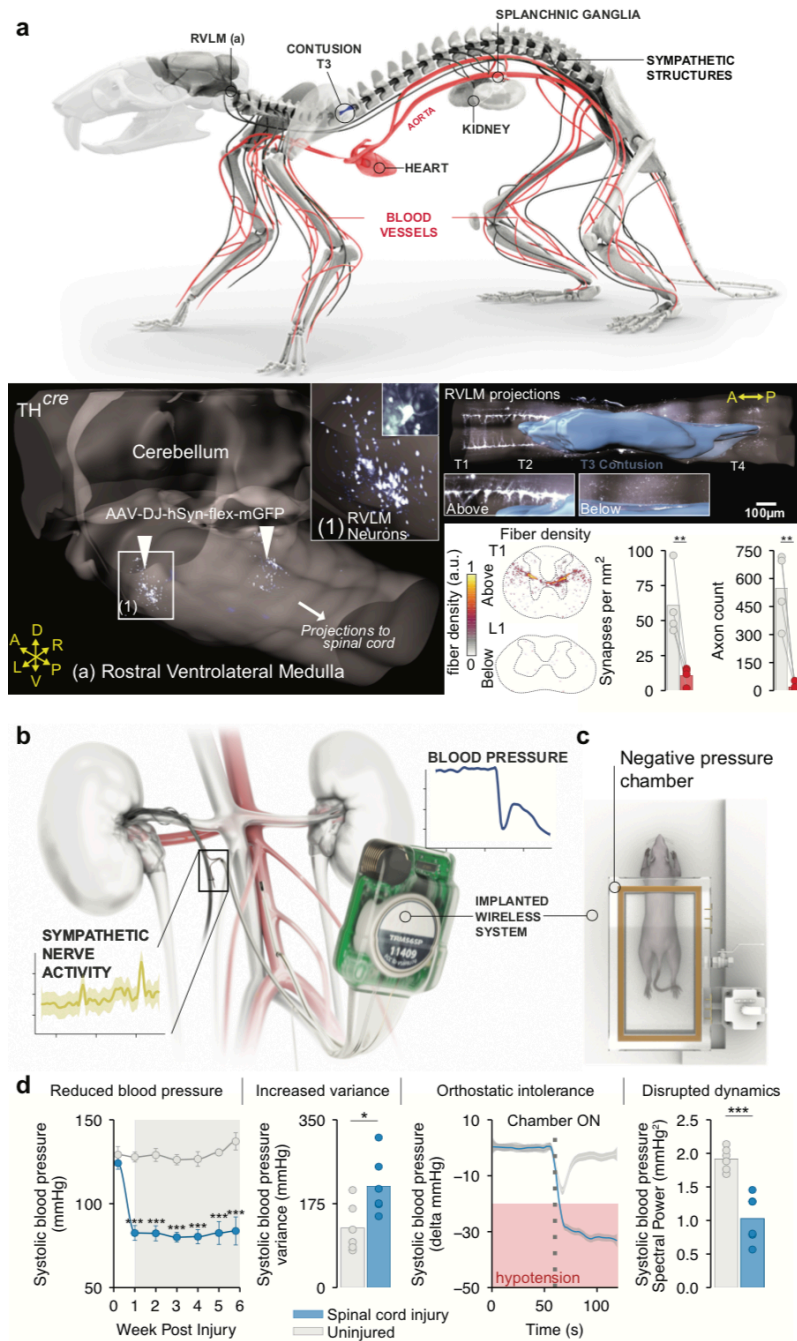
Fig. 1 | Preclinical model overview

a, Rodent experimental model. RVLM TH[ON] neurons and their projections after SCI. Barplots report mean fiber density above and below SCI (n = 4) (paired one-tailed t-test; t = 5.08; $P = 0.007$) and synapses (paired one-tailed t-test; t = 4.64; $P = 0.009$).

b, Wireless telemetry system to record hemodynamics and sympathetic nerve activity 24/7.

c, Negative pressure chamber to simulate an orthostatic challenge.

d, Resting blood pressure before and for 6 weeks post-injury (n = 6, two-way repeated measures ANOVA, Tukey's honestly significant difference (HSD); $F_{(1,6)\text{interaction}} = 7.05$; $P = 1.10e^{-05}$; all post-hoc < 0.001; mean ± SEM). Barplots report hemodynamic variance (n = 6, independent samples one-tailed t-test; t = 2.70; $P = 0.011$) and low frequency pressure dynamics (n = 6, independent samples one-tailed t-test; t = 5.51; $P = 0.0004$). The line plot illustrates orthostatic intolerance after injury and when exposed to lower body negative pressure. $*P < 0.05$; $**P < 0.01$; $***P < 0.001$.

EES engages the sympathetic circuitry to modulate hemodynamics

Clinical observations reported pressor responses when applying EES over lumbosacral segments[22-25], but the mechanisms underlying these responses remain unknown. We reasoned that understanding these mechanisms would be necessary to develop a therapy that manages hemodynamic instability with maximal efficacy.

We first investigated whether the location of EES was important to trigger pressor responses. We quantified the increase in blood pressure resulting from continuous EES (50Hz, motor threshold)[21] applied sequentially to each spinal segment, from T6 to L1. The pressor response to EES followed a Gaussian distribution that peaked around the low thoracic segments (**Fig. 2a** and **Extended Data Fig. 3c-d**). These responses were observed within a few hours after SCI and throughout the chronic phase of injury (**Extended Data Fig. 3d**).

We then asked if this pressor response distribution matched the topological organisation of the sympathetic circuitry[29]. To expose the anatomical distribution of sympathetic pre-ganglionic neurons in the spinal cord, we injected a retrograde tracer in the splanchnic sympathetic ganglia, which can control blood pressure (**Extended Data Fig. 3a**). We found retrogradely-labelled neurons throughout the well-established spinal cord topology, but a peak concentration of neurons was identified in the caudal thoracic segments (**Fig. 2a** and **Extended Data Fig. 3b**). Pressor responses to EES linearly correlated with the density of these neurons, revealing a clear anatomical and functional enrichment at T11-T13 (**Fig. 2a and Extended Data Fig. 3e**). We named these segments the *hemodynamic hotspots*.

We next aimed to uncover the neural substrates recruited by EES that trigger pressor responses. We first modeled the electrical fields elicited by EES using our previously-validated finite element methods[30] that we complemented with magnetic resonance imaging, computerized-tomography, and anatomical reconstructions of the thoracic spine (**Fig. 2c**). Simulations predicted that EES primarily recruits large-diameter afferent fibers located in the posterior roots, but has no direct influence on intraspinal neurons nor efferent pathways from sympathetic pre-ganglionic neurons (**Extended Data Fig. 4a**).

To test this prediction, we asked whether the thoracic posterior roots projecting to the *hemodynamic hotspots* were necessary to elicit pressor responses with EES. We found that the progressive ablation of these roots led to the graded suppression of pressor responses (**Fig. 2c** and **Extended Data Fig. 4b**).

Previous clinical studies reported pressor responses when stimulating rostral lumbar segments[22-25], which appeared incongruent with our finding that pressor responses elicited by EES require the recruitment of the posterior roots projecting to the caudal thoracic segments (**Fig. 2a**). We thus studied the mechanisms that could explain these observations. Computer simulations suggested that EES applied at L2 can recruit the caudal thoracic posterior roots where they bend and pass through the inter-vertebral foramen. Indeed, ablation of the T12 posterior roots blunted the modest pressor responses elicited by EES applied at L2 (**Extended Data Fig.**

3f). These results suggest that the incidental recruitment of T12 posterior roots at the level of L2 may mediate the pressor responses observed in previous clinical studies[22-25].
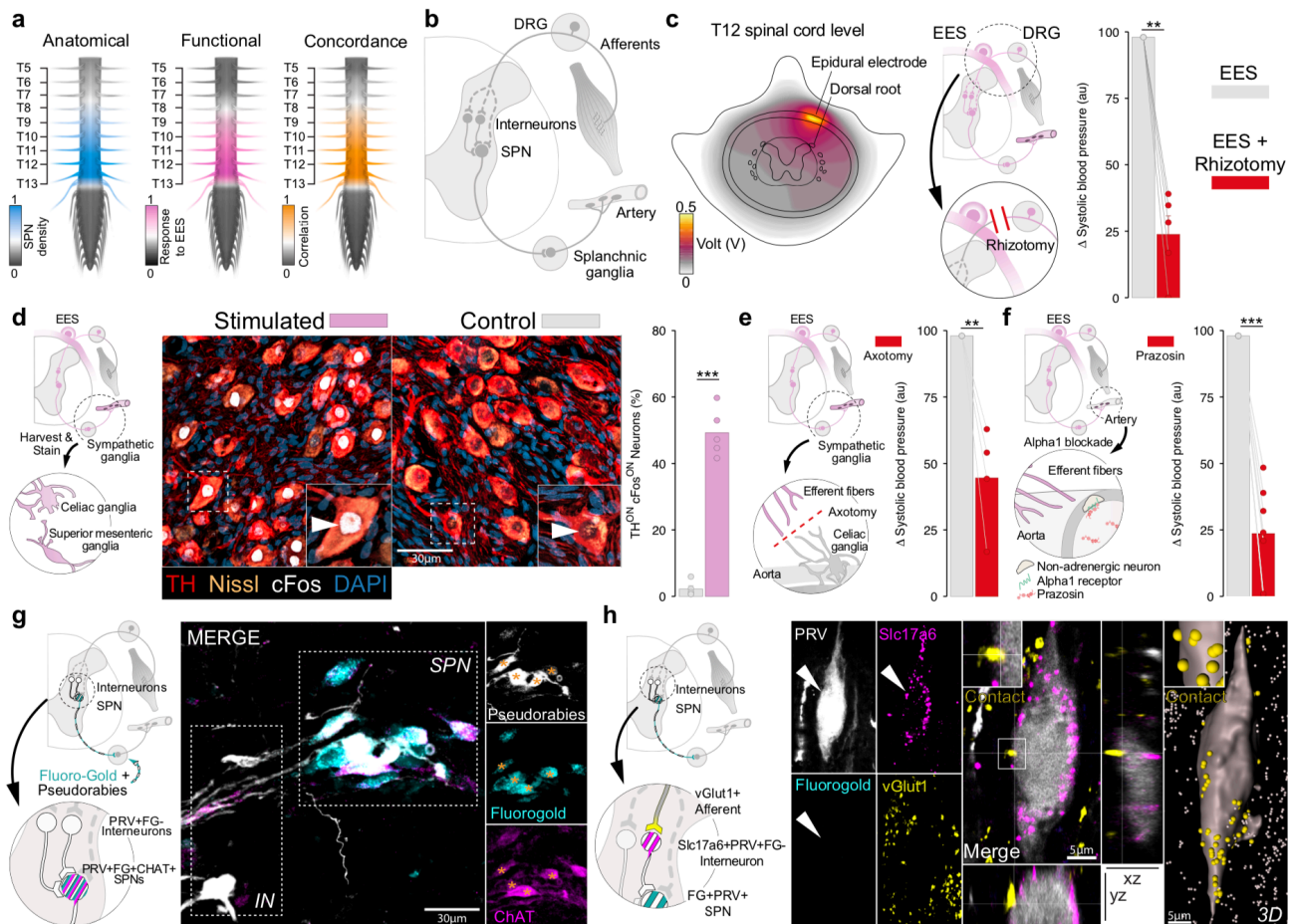

Fig. 2 | Mechanisms by which EES stabilizes hemodynamics

a, Intraspinal density of neurons retrogradely traced from the splanchnic ganglia one-month post-injury, amplitude of pressor responses to EES, and concordance between anatomical and functional datasets. Mean data are shown for n = 5 rats.

b, Hypothetical circuits activated by EES to elicit blood vessel constriction.

c, Electrical potentials elicited by EES. Barplots report pressor responses to EES before and after rhizotomy (n = 5, paired samples one-tailed t-test; 18.3 mmHg vs. 5.7 mmHg; t = 4.36; P = 0.006).

d, Fos expression in TH^{ON} neurons in the splanchnic ganglia. Barplot reports percentage of FOS^{ON} neurons (n = 5, independent samples one-tailed t-test; t = 13.96; P = 2.49e^{-05}).

e, Ablation of splanchnic efferents blunted the pressor response (n = 4, paired samples one-tailed t-test; 20.0 mmHg vs. 9.2 mmHg; t = -4.54; P = 0.0099).

f, alpha1 receptor blockade with prazosin blunted pressor responses (n = 5, paired samples one-tailed t-test; 18.0 mmHg vs. 5.7 mmHg; t = -5.59; P = 0.0007).

g, Trans-synaptic retrograde tracing revealing interneurons connected to splanchnic ganglia.

h, These interneurons express the excitatory marker *Slc17a6*, and receive vGlut1 synapses from proprioceptive afferents.

We next sought to confirm that EES engages sympathetic circuitry to elicit pressor responses. We tested whether EES recruits splanchnic sympathetic ganglion neurons, and if their efferent pathways trigger pressor responses. Delivering EES for 30 min induced a robust expression of the activity-dependent protein cFos in TH[ON] neurons located in splanchnic sympathetic ganglia (**Fig. 2d**). To ascertain their causal role, we expressed the light-sensitive eNpHR3.0 opsins[31] in these neurons using targeted injections of AAV5-hSyn-eNpHR3.0-YFP in splanchnic sympathetic ganglia. Silencing of these neurons with light or ablating their efferent pathways blunted the pressor response to EES (**Fig. 2e**, **Extended Data Fig. 5c-d**). These efferents release norepinephrine that induces constriction of blood vessels through the activation of alpha$_1$ receptors. We blocked these receptors with intravenous injections of prazosin[32], which reversibly suppressed responses to EES (**Fig. 2f**, **Extended Data Fig. 5e**).

These results show that the depolarization of afferent fibers in the posterior roots leads to the activation of splanchnic sympathetic ganglion neurons, which implied the existence of connections between afferent fibers and sympathetic pre-ganglionic neurons. We therefore labelled afferent projections with co-injections of AAV-DJ-hSyn-flex-mGFP-2A-Synaptophysin-mRuby and AAV-Cre into T12 dorsal root ganglia. We developed a pipeline to dynamically warp spinal cord contours to a histological atlas, allowing us to merge data from multiple tissue sections and rats (**Extended Data Fig. 4d**). Spatial analysis of merged matrices revealed an absence of afferent axons and synapses within the intermediolateral column that contains the vast majority of sympathetic pre-ganglionic neurons[29] (**Extended Data Fig. 4d**). We confirmed the absence of the traced synaptic projections onto sympathetic pre-ganglionic neurons by immunolabelling them with choline acetyltransferase (ChAT). Therefore, the connection between afferent fibers and sympathetic pre-ganglionic neurons likely involves an excitatory interneuron (**Extended Data Fig. 4c**). Time-dependent pseudorabies-mediated tracing revealed the presence of glutamatergic interneurons connected trans-synaptically to splanchnic sympathetic ganglionic neurons (**Fig. 2g**, **Extended Data Fig. 4d**). These interneurons were densely innervated by vGlut1[ON] synapses from proprioceptive neurons[33] **(Fig. 2h)**, supporting the existence of indirect connections between afferent fibers and sympathetic preganglionic neurons through an excitatory interneuron.

Together, these results identify key mechanisms underlying pressor responses elicited by EES. First, to maximize pressor responses, EES must target the spinal segments containing the highest density of sympathetic pre-ganglionic neurons that project to splanchnic neurons. Second, EES relies on the afferent fibers in the posterior roots to engage the sympathetic circuitry. Third, EES leads to the activation of splanchnic sympathetic ganglion neurons, which constrict blood vessels and increase blood pressure. These three key results provide a mechanistic framework to develop neurotechnologies to manage hemodynamic instability with EES.

Closed-loop control of hemodynamics through biomimetic stimulation
We exploited this knowledge to configure electronic dura mater (*e-dura*) implants[34] that targeted the posterior roots projecting to the six *hemodynamic hotspots*. Optimal electrode numbers and locations were identified using a genetic algorithm[12,21] implemented in the computational model.

We optimized the geometry of *e-dura* implants to conform to the curved topology of the thoracic spinal column (**Extended Data Fig. 6a-c**).

Neuromodulation strategies that mimic natural dynamics are more effective than unspecific protocols[12,21,35]. Moreover, non-physiological manipulation of hemodynamics may damage the central nervous system and circulatory system while predisposing to adverse events[36-38]. We therefore aimed to deliver EES patterns that mimic the natural dynamics of sympathetic circuitry activation. To capture these dynamics, we recorded sympathetic nerve activity and hemodynamics (**Extended Data Fig. 6d**). Feed-forward, artificial neural networks confirmed the disrupted link between hemodynamics and sympathetic circuitry after SCI (**Extended Data Fig. 6d**). Wavelet decomposition analysis[39] of blood pressure signals revealed that blue-light photostimulation of ChR2[ON] TH[ON] neurons located in the RVLM steers hemodynamics within specific frequency domains[40] confined around 0.4-1.0 Hz (**Fig. 3a**). Orthostatic challenges enhanced hemodynamic activity within the same frequency band in uninjured rats (**Fig. 3b**). This drive was permanently interrupted after SCI (**Fig. 3b**).
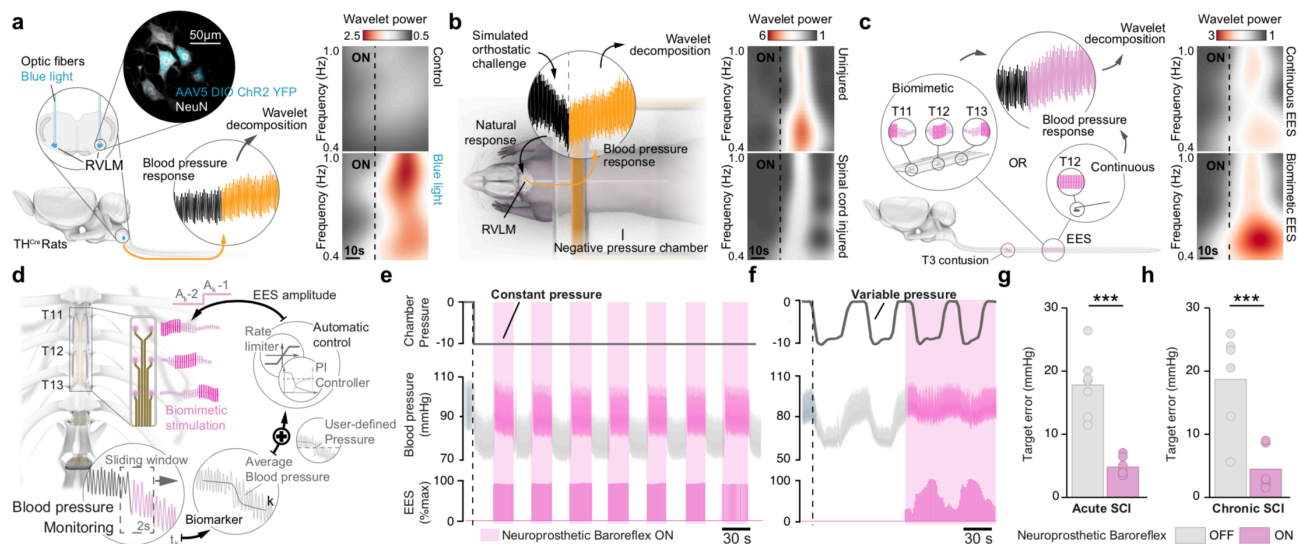

Fig. 3 | The *neuroprosthetic baroreflex* control hemodynamics

a, Targeted expression of ChR2 in TH[ON] neurons of the RVLM. Wavelet power spectrum when illuminating the RVLM with yellow (control) versus blue light (paired samples one-tailed t-test; t = 2.67; P = 0.028).

b, Wavelet spectrogram when inducing a simulated orthostatic challenge (n = 6; independent samples one-tailed t-test; t = 3.01; P = 0.0013).

c, Biomimetic stimulation protocols, composed of interleaved (2.5ms) EES (50Hz) propagating over the hemodynamic hotspots. Wavelet spectrogram in rats with SCI (n = 5, paired samples one-tailed t-test; t = 2.31; P = 0.041).

d, Pressure in the chamber, blood pressure and EES amplitude while the *neuroprosthetic baroreflex* is turned on and off sequentially. Representative example from one rat shown (n = 7 total).

e, Same variables as in **f** shown for cyclical changes in the pressure of the chamber. Representative example from one rat shown (n = 7 total).

Barplots reporting errors in blood pressure with respect to the user-defined target with the neuroprosthetic baroreflex on and off, tested in rats with **g,** acute (12 hours post-injury, n = 7, paired samples one-tailed t-tests; systolic blood pressure (SBP): t = -5.85, P= 5.50e[-04]) and **h,** chronic (6 weeks, n = 6, paired samples one-tailed t-tests; SBP: t = -3.84, P = 0.006) SCI.

We then measured the rostrocaudal transmission of descending sympathetic volleys (**Extended Data Fig. 6e**), which we quantified from the propagation of surface potentials over the *hemodynamic hotspots* in response to stimulation of RVLM neurons. We found a conduction delay of 2.5 ms between activation of adjacent hotspots.

We encoded these biometrics into EES protocols that mimic the spatial sequences, frequency contents and temporal profiles underlying natural sympathetic circuit activation. This biomimetic stimulation reinstated the natural dynamics of the system (**Fig. 3c**, **Extended Data Fig. 6f**), and triggered greater pressor responses than conventional EES protocols (**Extended Data Fig. 7a-b**).

The management of hemodynamic instability logically necessitates constant titration of EES. We found that biomimetic stimulation led to pressor responses that linearly correlated with EES amplitude (R^2 = 0.81; *P* = $1.02e^{-15}$). Therefore, we implemented a proportional-integral (PI) controller that modulated biomimetic EES protocols to target user-defined blood pressure levels in closed-loop[21] (**Fig. 3d**). This hemodynamic regulator updates EES amplitudes in real-time to prevent hypotension (**Fig. 3e-f**). We thus conceived a *neuroprosthetic baroreflex* that rapidly (1.15s 95% CI: 0.36-2.5) stabilized hemodynamics during transient, varying, and sustained orthostatic challenges, both after acute and chronic SCI (**Fig. 3e-h** and **Extended Data Fig. 7c-g**).

Translation of the neuroprosthetic baroreflex

We next asked whether this *neuroprosthetic baroreflex* could stabilize hemodynamics immediately after SCI using clinical-grade neurotechnologies (**Extended Data Fig. 8c**)[11,12]. We emulated neuro-intensive care in a non-human primate model that included general propofol-based anesthesia, an arterial pressure line, and artificial ventilation (**Fig. 4a, Extended Data Fig. 8a-b**).

We mapped pressor responses to EES across the thoracic and lumbar spinal cords of three Rhesus monkeys with acute complete upper-thoracic (T3) SCI, which confirmed the location of *hemodynamic hotspots* within the three most caudal thoracic segments (**Extended Data Fig. 9a-b**).

To modulate these *hemodynamic hotspots*, we designed *e-dura* implants[34] with electrode configurations that targeted the left and right posterior roots of T10, T11, and T12 segments. We scaled the implants developed for rats to the anatomical features of Rhesus monkeys, measured in three animals (**Extended Data Fig. 9c**). We connected these *e-dura* implants to a clinical-grade implantable pulse generator with wireless communication modules and custom-made software interfaces that enable real–time control over spatial locations, temporal sequences, and amplitudes of EES[12]. We injected all the features of the *neuroprosthetic baroreflex* within this versatile stimulation platform (**Extended Data Fig. 8c**).

The SCI induced an immediate spike in blood pressure, rapidly followed by pronounced hypotension reminiscent of life-threatening hemodynamic instability observed acutely in humans with SCI (**Extended Data Fig. 8d-e**).

As early as a few hours after the SCI, the *neuroprosthetic baroreflex* instantly normalized blood pressure, stabilizing hemodynamics for extensive periods of time without the need for supervision (2'000 heartbeats shown in **Fig. 4b**). Contrary to closed-loop EES, pressor responses induced by continuous EES extinguished after a few heartbeats in this acute phase of SCI (**Extended Data Fig. 9g-h**). The *neuroprosthetic baroreflex* maintained hemodynamic stability despite pronounced orthostatic challenges induced in a negative pressure chamber adapted to monkeys (**Fig. 4c** and **Extended Data Fig. 9f,i**). During hemodynamic collapse, the *neuroprosthetic baroreflex* rescued hemodynamic stability (**Fig. 4d** and **Supplementary Video 1**).

Clinical implementation

We finally aimed to validate the key features of the *neuroprosthetic baroreflex* in a patient presenting with a chronic clinically complete (American Spinal Injury Association Impairment Scale A) cervical SCI that led to debilitating, medically-refractory orthostatic hypotension (**Extended Data Fig. 10a**).

A paddle electrode array was surgically positioned below the T10 and T11 vertebral bodies that contain the posterior roots entering lower thoracic segments (**Extended Data Fig. 10a**). Computer simulations predicted the optimal electrode configurations[12] to target the *hemodynamic hotspots* identified in preclinical models (**Fig. 4e**). EES induced robust pressor responses (**Fig. 4f**), whereas stimulation delivered more caudally or over electrodes non-specific for the posterior roots (midline) was comparatively far less effective (**Extended Data Fig. 10c-d**). These results reinforced our conclusions that EES recruits the afferent fibers in the posterior roots to engage the sympathetic circuitry. EES increased sympathetic nerve activity and normalized circulating levels of norepinephrine, which confirmed the activation of the sympathetic circuitry (**Fig. 4g**).

We then asked whether EES could regulate hemodynamics in closed-loop. As observed in preclinical models, we found a linear relationship between EES amplitudes and pressor responses (**Extended Data Fig. 10e**). Closed-loop adjustment of EES amplitude led to real-time hemodynamic stabilization during orthostatic challenges on a tilt-table (**Fig. 4h** and **Extended Data Fig. 10f-g**).

Long-term implementation of EES enabled the permanent cessation of medical treatments for hemodynamic stabilization, increased participation in verticalized motor rehabilitation, and abolished the clinical burden of orthostatic hypotension (**Extended Data Fig. 10h and Supplementary Video 2**).
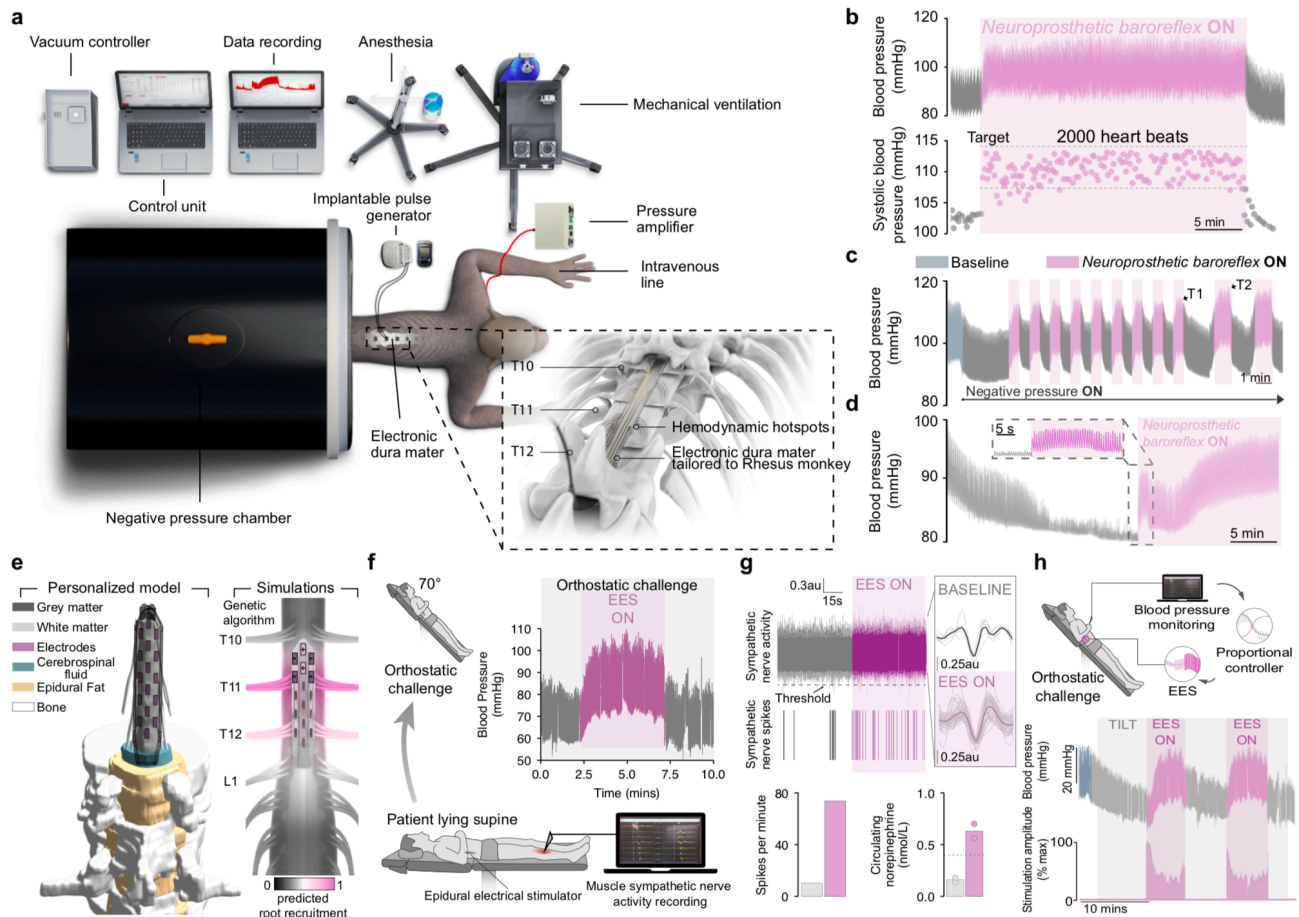
Fig. 4 | Translation of the _neuroprosthetic baroreflex_

a, Neurointensive care unit for monkeys with acute complete upper thoracic SCI, placed in a negative pressure chamber. The _neuroprosthetic baroreflex_ is implemented using clinical-grade technologies operated with a custom-made software.

c, Blood pressure with the _neuroprosthetic baroreflex_ on for 2000 heartbeats.

d, Same experiments as in Figure 3. T1 = first target, T2 = second target.

e, Blood pressure collapse, rescued by the _neuroprosthetic baroreflex_.

f, Computational model of the human participant, including predicted spatial configurations to target the cardiovascular hotspots.

g, Orthostatic challenge on a tilt table. Pressor response with EES.

h, Muscle sympathetic nerve activity (MSNA) recording from the peroneal nerve without and with EES. Barplots report MSNA spike rates and levels of circulating norepinephrine. Horizontal dotted line represents the reference range minimum.

i, Pressor responses during closed-loop EES concomitant to orthostatic challenges.

DISCUSSION

We developed and validated an ultrafast, highly-reliable _neuroprosthetic baroreflex_ that precisely stabilizes hemodynamics in the acute and chronic phases of SCI. Central to this development was a novel heuristic preclinical model of hemodynamic instability that enabled the identification of the topology and dynamics of natural sympathetic circuit activation. We combined this fundamental knowledge with a new understanding of the key mechanisms through which EES activates the sympathetic circuitry to conceive biomimetic protocols that obey guidelines for

ecoprosthetic designs[41]. The evolutionary conservation of the ancestral sympathetic circuitry enabled straightforward translation of these protocols from rats to non-human primates to humans.

We implemented this *neuroprosthetic baroreflex* within an implantable stimulation platform that we previously used to restore walking in humans with paralysis[12]. We validated this *neuroprosthetic baroreflex* in non-human primates. Experiments in one patient with tetraplegia indicated that the human spinal cord responds effectively to the key features of this treatment. Therefore, this clinical-grade investigational device will now enable clinical trials to evaluate the safety and therapeutic efficacy of the *neuroprosthetic baroreflex* in the acute, sub-acute and chronic phases of SCI.

The *neuroprosthetic baroreflex* triggered well-controlled and reversible increases in blood pressure. Therefore, these pressor responses must be distinguished from uncontrolled, life-threatening episodes of hypertension, known as autonomic dysreflexia[42,43]. The controllability of the *neuroprosthetic baroreflex* alleviates the concern of triggering uncontrolled hypertensive episodes, but it remains unclear whether the long-term use of the *neuroprosthetic baroreflex* would not exacerbate the incidence of autonomic dysreflexia. While future studies will need to investigate this risk, historical case studies suggest that chronic EES may instead mitigate autonomic dysreflexia[44].

In parallel, it is imperative to develop a fully implantable system combining a paddle lead targeting the *hemodynamic hotspots,* an arterial blood pressure monitoring unit, and a closed-loop stimulation platform to implement all the features of the *neuroprosthetic baroreflex*. The *neuroprosthetic baroreflex* foreshadows a new era in the clinical management of SCI.

DATA AVAILABILITY
Data that support the findings and software routines developed for the data analysis will be made available upon reasonable request to the corresponding author.

ONLINE CONTENT
Any methods, additional references, Nature Research reporting summaries, source data, statements of data availability and associated accession codes are available at:

REFERENCES

1. Squair, J. W., Phillips, A. A., Harmon, M. & Krassioukov, A. V. Emergency management of autonomic dysreflexia with neurologic complications. *Can. Med. Assoc. J.* **188,** 1100–1103 (2016).
2. Readdy, W. J. *et al.* Complications and outcomes of vasopressor usage in acute traumatic central cord syndrome. *J Neurosurg Spine* **23,** 574–580 (2015).
3. Inoue, T., Manley, G. T., Patel, N. & Whetstone, W. D. Medical and surgical management after spinal cord injury: vasopressor usage, early surgerys, and complications. *J. Neurotrauma* **31,** 284–291 (2014).
4. Squair, J. W. *et al.* Spinal cord perfusion pressure predicts neurologic recovery in acute spinal cord injury. *Neurology* **89,** 1660–1667 (2017).
5. Squair, J. W. *et al.* Empirical targets for acute hemodynamic management of individuals with spinal cord injury. *Neurology* **93,** e1205–e1211 (2019).
6. Cragg, J. J., Noonan, V. K., Krassioukov, A. & Borisoff, J. Cardiovascular disease and spinal cord injury: results from a national population health survey. *Neurology* **81,** 723–728 (2013).
7. Wu, J.-C. *et al.* Increased risk of stroke after spinal cord injury: a nationwide 4-year follow-up cohort study. *Neurology* **78,** 1051–1057 (2012).
8. Illman, A., Stiller, K. & Williams, M. The prevalence of orthostatic hypotension during physiotherapy treatment in patients with an acute spinal cord injury. *Spinal Cord* **38,** 741–747 (2000).
9. Carlozzi, N. E. *et al.* Impact of blood pressure dysregulation on health-related quality of life in persons with spinal cord injury: development of a conceptual model. *Arch. Phys. Med. Rehabil.* **94,** 1721–1730 (2013).
10. Furlan, J. C., Fehlings, M. G., Shannon, P., Norenberg, M. D. & Krassioukov, A. V. Descending vasomotor pathways in humans: correlation between axonal preservation and cardiovascular dysfunction after spinal cord injury. *J. Neurotrauma* **20,** 1351–1363 (2003).
11. Capogrosso, M. *et al.* A brain-spine interface alleviating gait deficits after spinal cord injury in primates. *Nature* **539,** 284–288 (2016).
12. Wagner, F. B. *et al.* Targeted neurotechnology restores walking in humans with spinal cord injury. *Nature* **563,** 65–71 (2018).
13. Saadoun, S., Chen, S. & Papadopoulos, M. C. Intraspinal pressure and spinal cord perfusion pressure predict neurological outcome after traumatic spinal cord injury. *J. Neurol. Neurosurg. Psychiatry* jnnp-2016-314600 (2016).
14. Vale, F. L., Burns, J., Jackson, A. B. & Hadley, M. N. Combined medical and surgical treatment after acute spinal cord injury: results of a prospective pilot study to assess the merits of aggressive medical resuscitation and blood pressure management. *J. Neurosurg.* **87,** 239–246 (1997).
15. Rawlings, A. M. *et al.* Association of orthostatic hypotension with incident dementia, stroke, and cognitive decline. *Neurology* **91,** e759–e768 (2018).

16. Phillips, A. A., Krassioukov, A. V., Ainslie, P. N. & Warburton, D. E. R. Baroreflex function after spinal cord injury. *J. Neurotrauma* **29,** 2431–2445 (2012).

17. Phillips, A. A., Krassioukov, A. V., Ainslie, P. N. & Warburton, D. E. R. Perturbed and spontaneous regional cerebral blood flow responses to changes in blood pressure after high-level spinal cord injury: the effect of midodrine. *J. Appl. Physiol.* **116,** 645–653 (2014).

18. Courtine, G. *et al.* Transformation of nonfunctional spinal circuits into functional states after the loss of brain input. *Nat. Neurosci.* **12,** 1333–1342 (2009).

19. Angeli, C. A. *et al.* Recovery of Over-Ground Walking after Chronic Motor Complete Spinal Cord Injury. *N. Engl. J. Med.* **379,** 1244–1250 (2018).

20. Gill, M. L. *et al.* Neuromodulation of lumbosacral spinal networks enables independent stepping after complete paraplegia. *Nat. Med.* **24,** 1677–1682 (2018).

21. Wenger, N. *et al.* Spatiotemporal neuromodulation therapies engaging muscle synergies improve motor control after spinal cord injury. *Nat. Med.* **22,** 138–145 (2016).

22. West, C. R. *et al.* Association of epidural stimulation with cardiovascular function in an individual with spinal cord injury. *JAMA Neurol.* **75,** 630–632 (2018).

23. Harkema, S. J. *et al.* Epidural spinal cord stimulation training and sustained recovery of cardiovascular function in individuals with chronic cervical spinal cord injury. *JAMA Neurol.* **75,** 1569–1571 (2018).

24. Harkema, S. J. *et al.* Normalization of blood pressure with spinal cord epidural stimulation after severe spinal cord injury. *Front. Hum. Neurosci.* **12,** 83 (2018).

25. Darrow, D. *et al.* Epidural Spinal Cord Stimulation Facilitates Immediate Restoration of Dormant Motor and Autonomic Supraspinal Pathways after Chronic Neurologically Complete Spinal Cord Injury. *J. Neurotrauma* **36,** 2325–2336 (2019).

26. Grimm, D. *et al.* In vitro and in vivo gene therapy vector evolution via multispecies interbreeding and retargeting of adeno-associated viruses. *J. Virol.* **82,** 5887–5911 (2008).

27. Witten, I. B. *et al.* Recombinase-driver rat lines: tools, techniques, and optogenetic application to dopamine-mediated reinforcement. *Neuron* **72,** 721–733 (2011).

28. Tomer, R., Ye, L., Hsueh, B. & Deisseroth, K. Advanced CLARITY for rapid and high-resolution imaging of intact tissues. *Nat. Protoc.* **9,** 1682–1697 (2014).

29. Strack, A. M., Sawyer, W. B., Marubio, L. M. & Loewy, A. D. Spinal origin of sympathetic preganglionic neurons in the rat. *Brain Res.* **455,** 187–191 (1988).

30. Capogrosso, M. *et al.* A computational model for epidural electrical stimulation of spinal sensorimotor circuits. *J. Neurosci.* **33,** 19326–19340 (2013).

31. Gradinaru, V., Thompson, K. R. & Deisseroth, K. eNpHR: a Natronomonas halorhodopsin enhanced for optogenetic applications. *Brain Cell Biol* **36,** 129–139 (2008).

32. Phillips, A. A., Elliott, S. L., Zheng, M. M. Z. & Krassioukov, A. V. Selective alpha adrenergic antagonist reduces severity of transient hypertension during sexual stimulation after spinal cord injury. *J. Neurotrauma* **32,** 392–396 (2015).

33. Beauparlant, J. *et al*. Undirected compensatory plasticity contributes to neuronal dysfunction after severe spinal cord injury. *Brain* **136,** 3347–3361 (2013).
34. Minev, I. R. *et al*. Biomaterials. Electronic dura mater for long-term multimodal neural interfaces. *Science* **347,** 159–163 (2015).
35. Formento, E. *et al*. Electrical spinal cord stimulation must preserve proprioception to enable locomotion in humans with spinal cord injury. *Nat. Neurosci.* **21,** 1728–1741 (2018).
36. Cornwell, W. K. *et al*. Restoration of Pulsatile Flow Reduces Sympathetic Nerve Activity Among Individuals With Continuous-Flow Left Ventricular Assist Devices. *Circulation* **132,** 2316–2322 (2015).
37. Purohit, S. N., Cornwell, W. K., Pal, J. D., Lindenfeld, J. & Ambardekar, A. V. Living Without a Pulse: The Vascular Implications of Continuous-Flow Left Ventricular Assist Devices. *Circ Heart Fail* **11,** e004670 (2018).
38. Cheng, A., Williamitis, C. A. & Slaughter, M. S. Comparison of continuous-flow and pulsatile-flow left ventricular assist devices: is there an advantage to pulsatility? *Ann Cardiothorac Surg* **3,** 573–581 (2014).
39. Saleem, S. *et al*. Wavelet decomposition analysis is a clinically relevant strategy to evaluate cerebrovascular buffering of blood pressure after spinal cord injury. *Am. J. Physiol. Heart Circ. Physiol.* **314,** H1108–H1114 (2018).
40. Phillips, A. A., Warburton, D. E. R., Ainslie, P. N. & Krassioukov, A. V. Regional neurovascular coupling and cognitive performance in those with low blood pressure secondary to high-level spinal cord injury: improved by alpha-1 agonist midodrine hydrochloride. *J. Cereb. Blood Flow Metab.* **34,** 794–801 (2014).
41. Courtine, G. & Bloch, J. Defining ecological strategies in neuroprosthetics. *Neuron* **86,** 29–33 (2015).
42. Phillips, A. A. & Krassioukov, A. V. Contemporary Cardiovascular Concerns after Spinal Cord Injury: Mechanisms, Maladaptations, and Management. *J. Neurotrauma* **32,** 1927–1942 (2015).
43. Phillips, A. A. & Krassioukov, A. V. in *Neurological aspects of spinal cord injury* (eds. Weidner, N., Rupp, R. & Tansey, K. E.) 325–361 (Springer International Publishing, 2017). doi:10.1007/978-3-319-46293-6_14
44. Richardson, R. R., Cerullo, L. J. & Meyer, P. R. Autonomic hyper-reflexia modulated by percutaneous epidural neurostimulation: a preliminary report. *Neurosurgery* **4,** 517–520 (1979).

Author Contributions.
J.W.S., M.G., Lo.M., J.E.S., N.C., A.B., M.A.A., N.D.J., A.L., L. Mc., I.J C.M., J.G., Z.K.S., C.K., K.B., J.R., Q.B. E.M.M., and AAP performed the rodent experiments and analyzed the data. A.R. and Ma.C. performed computational experiments. J.B., G.C., E.B., Y.C., and L.Q. conducted the non-human primate experiments. J.W.S., R.D., S.K., C.M., F.B.W., R.B., N.B., E.M.M, T.D. G.S., X.K., N.V., F.F., S.P.L, G.C, and A.A.P designed hardware and software for neurostimulation. A.V.I., P.J.M., B.V., B.S., R.R., R.C, E.S., S.D, S.B, A.V.I., I.R, A.A.P performed the human experiments and analyzed the data. G.C. and A.A.P. conceived and supervised the study. J.W.S, G.C., and A.A.P. wrote the paper, and all the authors contributed to its editing.

Supplementary information is available for this paper at.
Correspondence and requests for materials should be addressed to G.C or A.A.P.
Reprints and permissions information is available at http://www.nature.com/reprints

Step 1 (a)

Classic models of hemodynamic instability do not apply in rodents

T3 Contusion — Orthostatic challenge — 28d
n = 4 rats

Orthostatic challenge — 90°

Systolic blood pressure | Mean arterial pressure | Diastolic blood pressure
ΔPressure (mmHg)
TILT
Threshold
Time (minutes)

Step 2 (b)

TH^{ON} projections from the rostral ventrolateral medulla were visualized with CLARITY and nearly completely disrupted after spinal cord contusion

AAV-DJ-hSyn-flex-mGFP-2A-Syn-mRuby
CLARITY
RVLM
Below
Above
TH^{Cre} rats
n = 4 rats
T3 Contusion (400kDyn)

RVLM neurons
GFP
Projections to spinal cord
3D
synaptophysin-mruby
GFP
synaptophysin-mRuby
merge

RVLM projections
T3 Contusion
T1
T2
100μm

Fiber density
fiber density (a.u.)
Above
Below
T1
L1

Tract
SPN
synaptophysin-mRuby
10μm
Tract
Below contusion
SPN / GFP
SPN
synaptophysin-mRuby

Depletion of RVLM projections
Synapses per nm²
Axon count
Above
Below

Step 3 (c)

Overview of time course and injury model

Telemetry implantation — -7d — 0 — End-point — 42d
T3 Contusion
Assessments
Uninjured (n=6 rats)
Spinal cord injury (n=6 rats)

LESION SITES
GFAP
250μm
2%
3%
0.8%
1%
0.9%
1%
Spared tissues

Step 4 (d)

Implantation of wireless system for 24/7 monitoring

Blood pressure implantation
Aorta
IVC
Iliac artery

Microelectrodes sewn to renal nerve
Aorta
IVC
Renal nerve

Inferior vena cava
Aorta
Renal nerve
Telemetry device

Step 5 (e)

Automated and continuous data analysis

Continuous recordings in freely moving rat
Blood pressure
Sympathetic nerve activity

24/7 recording
Automated hourly backup
Upload
Automated analysis
RAW — CLEAN

Step 6 (f)

Natural history of hemodynamics

Chronic recordings
Filtering | Peak detection | Outlier detection

Recordings during SCI
Sympathethic nerve response | Blood pressure response

Weekly assessments
Chamber pressure | Hypotensive event severity | Blood pressure / chamber relationship

Step 7 (g)

Development of new model of simulated orthostatic challenge using servo-controlled negative pressure chamber in rodents

Controlled baseline recording | Induced hypotensive events of increasing severity | Long lasting induced hypotensive event

1 Wireless continuous hemodynamic monitoring
Blood pressure
Sympathetic nerve

2 Servo-controlled negative pressure induction
Chamber activation

17

Extended Data Figure 1. Development of a novel model of hemodynamic instability in rodents.

Step 1(a): We first tested the capacity for an orthostatic challenge to reduce blood pressure in rats 30 days after a T3 spinal cord injury ($n = 4$). Tilting rats 90 degrees upright did not lead to any reduction in systolic blood pressure (one-way repeated measures ANOVA; $F_3 = 0.612$; $P = 0.62$), diastolic blood pressure (one-way repeated measures ANOVA; $F_3 = 1.105$; $P = 0.40$), or mean arterial pressure (one-way repeated measures ANOVA; $F_3 = 0.915$; $P = 0.47$). Data are mean ± SEM.

Step 2(b): To confirm that our contusion model disrupted descending control of hemodynamics we used AAV-DJ-hSyn-flex-mGFP-2A-Synaptophysin-mRuby injected into the rostral ventrolateral medulla (RVLM) of tyrosine hydroxylase (TH)-Cre rats ($n = 4$) one month after T3 spinal cord injury. We found a near complete disruption of descending TH^{ON} sympatho-excitatory axons (paired one-tailed t-test; t = 5.08; $P = 0.007$) and synapses (paired one-tailed t-test; t = 4.64; $P = 0.009$) when comparing counts above and below the injury. Barplots represent the mean with raw data overlaid.

Step 3(c): Overview of the time-course used to examine the natural history of hemodynamic instability in uninjured ($n = 6$) and spinal cord injured animals ($n = 6$). Confirmation that the lesion site spared minimal white matter (identified using glial fibrillary acidic protein [GFAP]; mean = 2%).

Step 4(d): We implanted a wireless recording system to monitor hemodynamics and sympathetic nerve activity. A blood pressure cannula was inserted into the abdominal aorta and microelectrodes sutured to the sympathetic renal nerve.

Step 5(e): Data was recorded 24/7 and automatically uploaded to a server where automated analyses were triggered to quantify blood pressure and sympathetic nerve activity throughout the day and night.

Step 6(f): We established the natural history of hemodynamic instability by recording the response to spinal cord injury and automatically detecting outliers (see **Supplementary Online Methods,** *Hemodynamic and sympathetic nerve activity monitoring*) for blood pressure and sympathetic nerve activity data for a total of 7 weeks.

Step 7(g): Because rats do not exhibit hemodynamic instability in response to an orthostatic challenge (see Step 1(a)), we developed a servo-controlled negative pressure approach whereby animals are placed in a chamber and the pressure is dropped and monitored in closed loop (see **Supplementary Online Methods,** *Implementation of a simulated orthostatic challenge in rodents and non-human primates*).

*$P < 0.05$; **$P < 0.01$; ***$P < 0.001$.
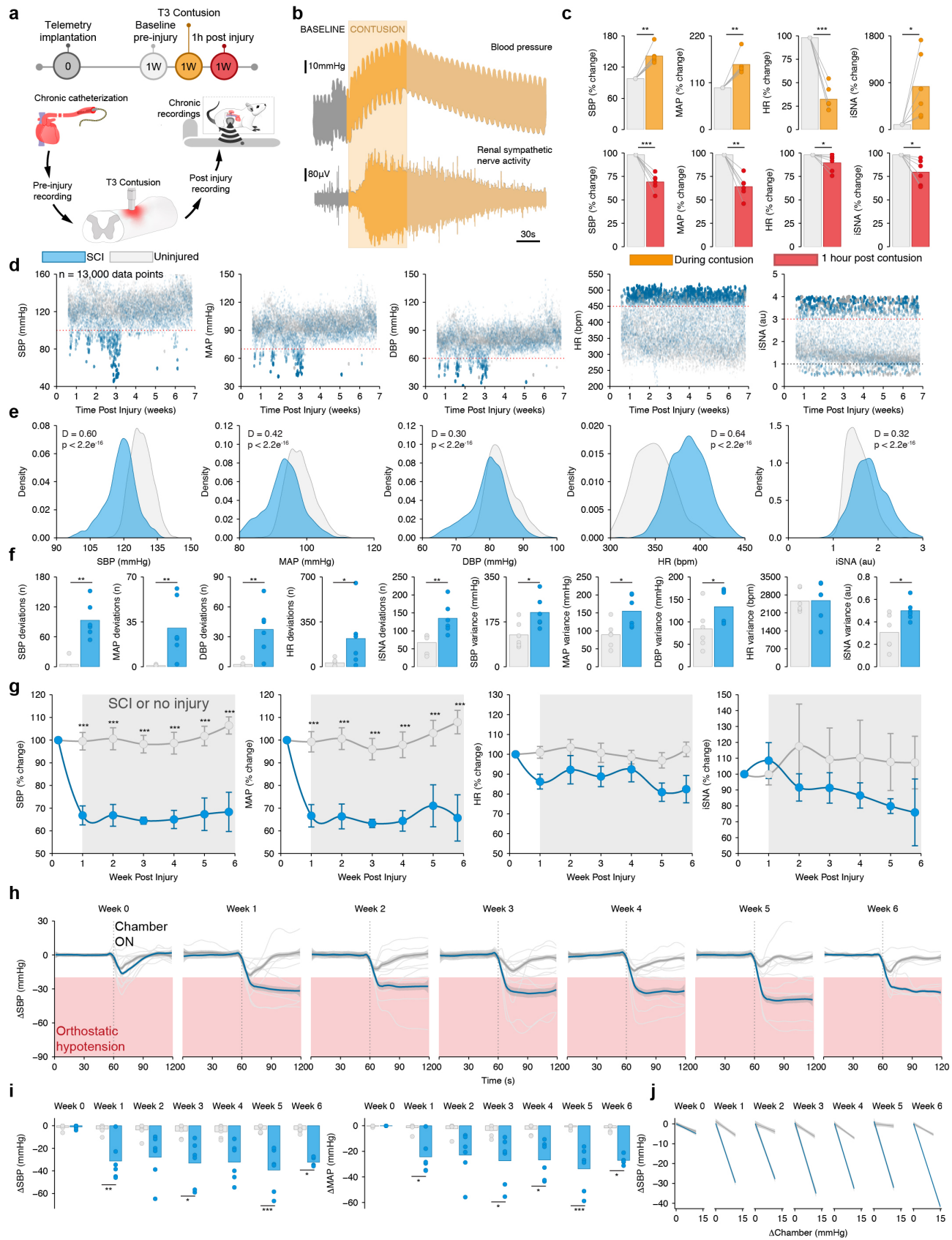
Extended Data Figure 2. Rodent model develops hemodynamic instability across the natural history of spinal cord injury.

a, We recorded hemodynamics and sympathetic nerve activity during and after the spinal cord contusion (n = 6).

b, We observed an immediate increase in blood pressure and sympathetic nerve activity following the onset of the contusion.

c, Quantifications revealed a significant increase in systolic blood pressure (paired one-tailed t-test; 91 mmHg vs. 128 mmHg; t = 5.40; P = 0.001) and mean arterial pressure (paired one-tailed t-test; 63 mmHg vs. 96 mmHg; t = 4.50; P = 0.003), a decrease in heart rate (paired one-tailed t-test; 309 bpm vs. 100 bpm; t = -10.26; P = $7.56e^{-05}$), and an increase in sympathetic nerve activity (paired one-tailed t-test; t = 2.26; P = 0.037) during contusion. These were followed by complete reversal after the contusion, where systolic blood pressure (paired one-tailed t-test; 116 mmHg vs. 79 mmHg; t = -5.97; P = 0.0009), mean arterial pressure (paired one-tailed t-test; 85 mmHg vs. 53 mmHg; t = -5.14; P = 0.002), sympathetic nerve activity (paired one-tailed t-test; t = -3.29; P = 0.011), and heart rate (paired one-tailed t-test; 350 bpm vs. 313 bpm; t = -2.91; P = 0.017) decreased compared to pre-injury.

d, We next established the natural history of hemodynamics using 24/7 recordings. We found that throughout the recording period animals with spinal cord injury deviated outside key thresholds representing 'normal' values (points scaled by size and transparency based on their deviation outside our set thresholds [dotted lines]).

e, We found a left-shift in the distribution of hemodynamic values, and a right-ward shift in heart rate values, indicating generally lower blood pressure, higher heart rate, and more aberrant sympathetic nerve activity (Kolmogorov-Smirnov test; all P < $2.2e^{-16}$).

f, Quantifications revealed an increase in the number of deviations for systolic blood pressure (independent samples one-tailed t-test; t = 5.92; P = 0.0005), diastolic blood pressure (independent samples one-tailed t-test; t = 3.68; P = 0.007), mean arterial pressure (independent samples one-tailed t-test; t = 3.23; P = 0.011), heart rate (independent samples one-tailed t-test; t = 2.0; P = 0.0499), and sympathetic nerve activity (independent samples one-tailed t-test; t = 3.20; P = 0.006). We additionally found an increase in the variance of systolic blood pressure (independent samples one-tailed t-test; t = 2.70; P = 0.011), diastolic blood pressure (independent samples one-tailed t-test; t = 2.01; P = 0.036), mean arterial pressure (independent samples one-tailed t-test; t = 2.85; P = 0.009), and sympathetic nerve activity (independent samples one-tailed t-test; t = 3.20; P = 0.006), fitting the criteria for hemodynamic instability after SCI.

g, Formal baseline recordings revealed that baseline systolic blood pressure (two-way repeated measures ANOVA; interaction effect $F_{6,1}$ = 7.05; P = $1.10e^{-05}$; all Tukey post-hoc P < 0.001) and mean arterial pressure (two-way repeated measures ANOVA; interaction effect $F_{6,1}$ = 4.93; P = 0.0004; all Tukey post-hoc P < 0.001) were reduced, in agreement with spontaneous 24/7 data recordings. Data are mean ± SEM.

h, We devised a closed-loop negative pressure system to mimic an orthostatic challenge in rats. Animals with spinal cord injury could not respond to decreasing pressures, whereas uninjured animals responded and slowly recovered. This response was consistent across all six weeks post injury and is contrasted against week 0 (no injury for both groups).

i, Quantification of this response revealed increased negative deltas for the spinal cord injury group for systolic blood pressure (two-way repeated measures ANOVA; interaction effect $F_{6,1}$ = 3.71; P =0.003; all Tukey post-hoc P < 0.05) and mean arterial pressure (two-way repeated measures ANOVA; interaction effect $F_{6,1}$ = 4.20; P = 0.001; all Tukey post-hoc P < 0.05).

j, After SCI we observed a time-dependent increase in the linear relationship between chamber pressure and blood pressure (likelihood ratio test of nested models; P < 0.001), indicating that hemodynamics cannot be stabilized during orthostatic challenge without a functioning baroreflex. In all panels, percent change is presented for clarity as needed, while all statistics are calculated from raw values. Bar plots represent the mean with raw data overlaid.

*P < 0.05; **P < 0.01; ***P < 0.001.

Abbreviations: iSNA: integrated sympathetic nerve activity; HR: heart rate; MAP: mean arterial pressure; SBP: systolic blood pressure; SCI: spinal cord injury.

Step 1 (a)

Electrical stimulation of splanchnic ganglia increases blood pressure

Step 2 (b)

Sympathetic pre-ganglionic neurons reach maximal density at T11 to T13 spinal segments

Step 3 (c)

Timeline of functional mapping experiments

Step 4 (d)

Functional mapping shows robust hemodynamic hotspots across time post-injury

Step 5 (e)

Functional and anatomical mappings show strong concordance

Step 6 (f)

Serendipitous clinical observations are likely due to off-target recruitment of low thoracic posterior roots when stimulating over the lumbar spinal cord

21

Extended Data Figure 3. Functional and anatomical mapping reveal hemodynamic hotspots preferentially enriched to respond to epidural electrical stimulation.

Step 1(a): We confirmed the role of the splanchnic ganglia in activating pressor responses. Electrical stimulation of splanchnic ganglia led to pressure responses that linearly increased with the stimulation amplitude (n = 4, linear mixed modelling; all R^2 > 0.71; all P < 6.72e^{-12}). These relationships were robust across systolic blood pressure, diastolic blood pressure, and mean arterial pressure.

Step 2(b): Retrograde tracing of splanchnic ganglia using fluorogold labelled sympathetic pre-ganglionic neurons, which we confirmed using Choline Acetyltransferase (ChAT) staining. Successful injection was confirmed in splanchnic ganglia by colocalization of fluorogold with tyrosine hydroxylase (TH). We found a peak density in the number of sympathetic pre-ganglionic neurons projecting to splanchnic ganglia in the lower thoracic segments.
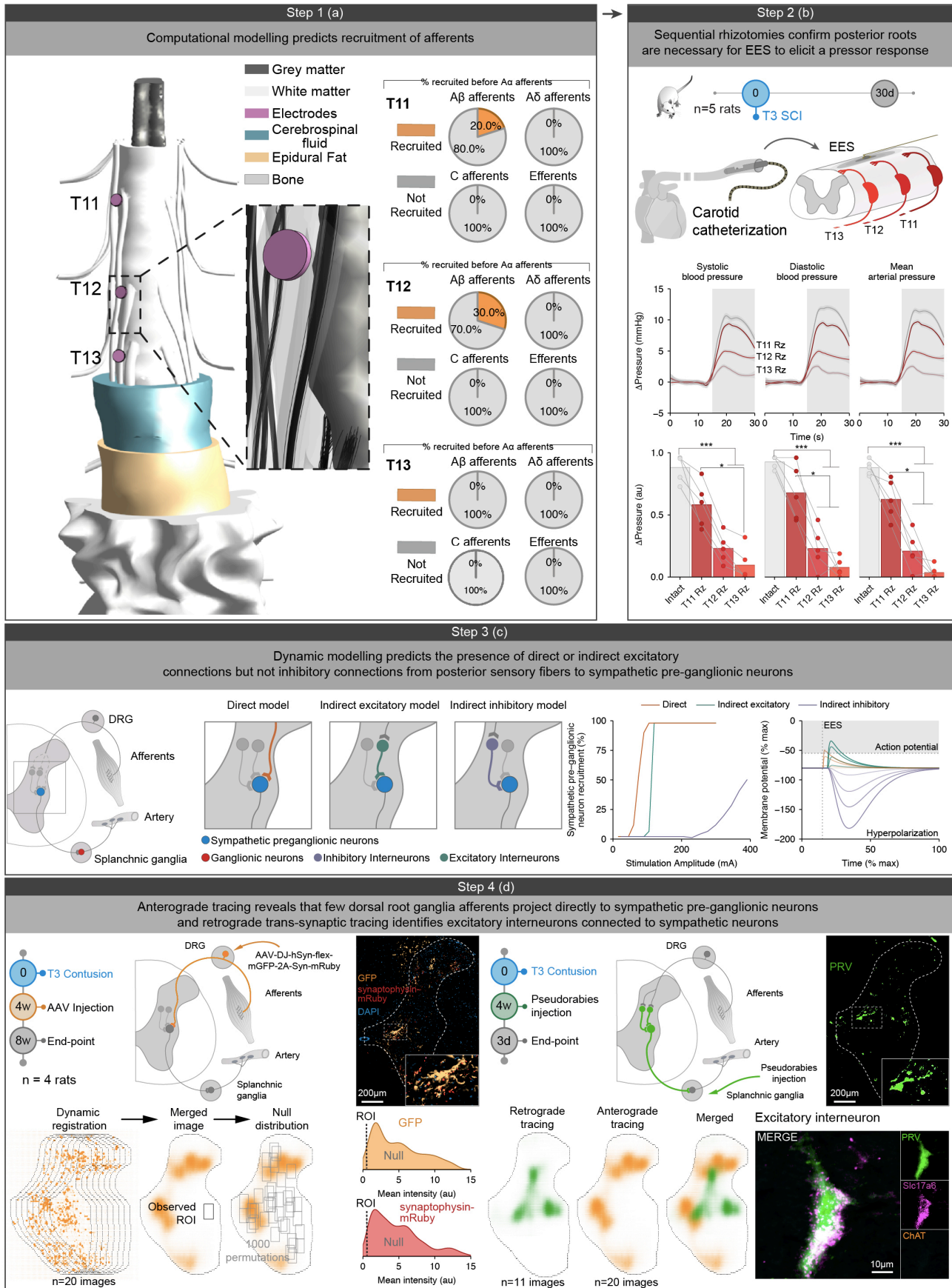
Step 3(c): We next completed functional mapping of the spinal cord by iterating through each segment and stimulating epidurally to activate pressor responses. We completed these experiments in animals one-hour post-injury (acute, n = 3), one-week post-injury (sub-acute, n = 3), two-weeks post-injury (intermediate, n = 5), and four-weeks post-injury (chronic, n = 5). We recorded blood pressure using a terminal carotid catheterization preparation, and calculated the peak change in blood pressure during the stimulation.

Step 4(d): We found that the response to targeted epidural electrical stimulation (EES) increased with time post-injury, and that there was a *hemodynamic hotspot* in the lower thoracic spinal cord.

Step 5(e): We found a linear relationship between the functional and anatomical mapping results, providing a clear rationale for the existence of the observed *hemodynamic hotspot* (linear modelling; all R^2 > 0.72; all P < 0.003).

Step 6(f): We used computational modelling (see **Extended Data Figure 4**) and found that lateral edge (near root entrance/exit) placement of electrodes resulted in preferential recruitment of T12, even with EES placed at L2. This was in contrast to more midline stimulation where we saw preferential recruitment off L2. Indeed, with electrodes placed with a subtle 'lateral shift' the shift in recruitment to T12 already begins. We reasoned this may be the mechanism by which serendipitous clinical observations were made. We confirmed this hypothesis using a rhizotomy experiment, whereby we cut the T12 root after stimulating with EES at L2 (n = 5). We found a significant blunting of the EES response in systolic blood pressure (paired one-tailed t-test; 10 mmHg vs. 6.9 mmHg; t = -3.95; P = 0.008), mean arterial pressure (paired one-tailed t-test; 9.9 mmHg; vs. 5.6 mmHg; t = -6.03; P = 0.002), and diastolic blood pressure (paired one-tailed t-test; 9.8 mmHg; vs. 5.3 mmHg; t = -5.90; P = 0.002). Bar plots represent the mean with raw data overlaid.

Abbreviations: ChAT: choline acetyltransferase; DBP: diastolic blood pressure; MAP: mean arterial pressure; SBP: systolic blood pressure; SCI: spinal cord injury; SPN: sympathetic pre-ganglionic neuron; EES: targeted epidural electrical spinal cord stimulation; TH: tyrosine hydroxylase.

Step 1 (a)

Computational modelling predicts recruitment of afferents

Grey matter
White matter
Electrodes
Cerebrospinal fluid
Epidural Fat
Bone

T11
% recruited before Aα afferents
Aβ afferents — Recruited 20.0% / 80.0%
Aδ afferents — 0% / 100%
C afferents — Not Recruited 0% / 100%
Efferents — 0% / 100%

T12
% recruited before Aα afferents
Aβ afferents — Recruited 30.0% / 70.0%
Aδ afferents — 0% / 100%
C afferents — Not Recruited 0% / 100%
Efferents — 0% / 100%

T13
% recruited before Aα afferents
Aβ afferents — Recruited 0% / 100%
Aδ afferents — 0% / 100%
C afferents — Not Recruited 0% / 100%
Efferents — 0% / 100%

Step 2 (b)

Sequential rhizotomies confirm posterior roots are necessary for EES to elicit a pressor response

n=5 rats / 0 T3 SCI / 30d

EES
Carotid catheterization
T13 T12 T11

Systolic blood pressure / Diastolic blood pressure / Mean arterial pressure
ΔPressure (mmHg)
T11 Rz / T12 Rz / T13 Rz
Time (s)

ΔPressure (au)
Intact / T11 Rz / T12 Rz / T13 Rz
*** *

Step 3 (c)

Dynamic modelling predicts the presence of direct or indirect excitatory connections but not inhibitory connections from posterior sensory fibers to sympathetic pre-ganglionic neurons

DRG
Afferents
Artery
Splanchnic ganglia

Direct model / Indirect excitatory model / Indirect inhibitory model

Sympathetic preganglionic neurons
Ganglionic neurons
Inhibitory Interneurons
Excitatory Interneurons

Direct / Indirect excitatory / Indirect inhibitory
Sympathetic pre-ganglionic neuron recruitment (%)
Stimulation Amplitude (mA)

EES
Action potential
Membrane potential (% max)
Hyperpolarization
Time (% max)

Step 4 (d)

Anterograde tracing reveals that few dorsal root ganglia afferents project directly to sympathetic pre-ganglionic neurons and retrograde trans-synaptic tracing identifies excitatory interneurons connected to sympathetic neurons

0 T3 Contusion
4w AAV Injection
8w End-point
n = 4 rats

DRG
AAV-DJ-hSyn-flex-mGFP-2A-Syn-mRuby
Afferents
Artery
Splanchnic ganglia

GFP synaptophysin-mRuby DAPI
200μm

0 T3 Contusion
4w Pseudorabies injection
3d End-point

DRG
Afferents
Artery
Pseudorabies injection
Splanchnic ganglia

PRV
200μm

Dynamic registration → Merged image → Null distribution
Observed ROI
1000 permutations
n=20 images

ROI GFP Null
Mean intensity (au)
ROI synaptophysin-mRuby Null
Mean intensity (au)

Retrograde tracing / Anterograde tracing / Merged
n=11 images / n=20 images

Excitatory interneuron
MERGE
PRV
Slc17a6
ChAT
10μm

23

Extended Data Figure 4. Epidural electrical stimulation induces pressor responses through the recruitment of posterior afferents and excitatory interneurons.

Step 1(a): We developed a hybrid computational model based on real anatomical structures generated through high-resolution CT and MRI scans. This model combines a geometrically realistic 3D finite element model of the spinal cord with realistic compartmental cable models of all afferents, efferents and some interneurons. We established a computational pipeline to obtain anisotropic tissue property maps, discretize the model, perform simulations using an electro-quasi-static solver and couple these simulations with NEURON-based electrophysiology models (Sim4Life by ZMT, www.zurichmedtech.com). We investigated the recruitment patterns of various afferent and efferent fibers within the spinal cord structure. We found that stimulation over the dorsal aspect of the spinal cord led to high levels of recruitment of major afferents, prior to any recruitment of efferent neurons directly from the stimulation. This suggested that epidural electrical stimulation activates pressor responses by recruiting afferents.

Step 2(b): Next, we experimentally tested the hypothesis that pressor responses induced by EES were dependent on afferent activation. We completed successive dorsal rhizotomies at T11, T12, and T13 and found a graded reduction in the response to stimulation (one-way ANOVA; all $P < 0.001$; post-hoc results indicated), with the largest decrease when removing T12, consistent with our functional and anatomical mapping results. Grey box indicates stimulation. Bar plots represent the mean with raw data overlaid.

Step 3(c): Next, we developed a NEURON-based spiking neural network model composed of integrate-and-fire neurons to predict the presence of direct, indirect excitatory, and indirect inhibitory connections. Indirect inhibitory connections resulted in poor sympathetic pre-ganglionic neuron recruitment (left panel) and in the minimization of membrane potentials in response to increasing stimulation amplitude (right panel; various stimulation amplitudes indicated by alpha; action potential threshold indicated by horizontal dotted line; stimulation onset indicated by vertical dotted line). This suggested that pressor responses to EES likely are mediated by either direct, monosynaptic connections between afferents and sympathetic pre-ganglionic neurons or by indirect circuits including excitatory interneurons.

Step 4(d): We completed anterograde tracing of the dorsal root ganglia. Using dynamic image registration we generated a digital dorsal horn whereby we could select a region of interest (ROI; grey box) and determine the mean intensity ('Observed ROI') of either axons (orange) or synapses (red). Using 1000 bootstraps of random ROIs as a null distribution we found a depletion of axons (empirical $P = 0.019$) and synapses (empirical $P = 0.001$) in the intermediolateral column. We confirmed this result by counting neurons with appositional synapses on ChAT[ON] neurons in the ventral horn versus the lateral horn and found a similar statistical depletion ($n = 10$ images, 294 neurons; Fisher's exact test; OR: 0.082; $P < 2.2e^{-16}$). This suggested that the most likely circuit mediating these responses instead included an excitatory interneuron. We therefore completed retrograde trans-synaptic tracing and found interneurons trans-synaptically connected to splanchnic ganglia that were Slc17a6 positive, and had Vglut1 synaptic puncta in their immediate vicinity (see **Figure 2**), suggesting direct connections with large diameter afferents.

$*P < 0.05$; $**P < 0.01$; $***P < 0.001$.

Abbreviations: ChAT: choline acetyltransferase; PRV: pseudorabies; ROI: region of interest; Rz: rhizotomy; EES: targeted epidural spinal stimulation.
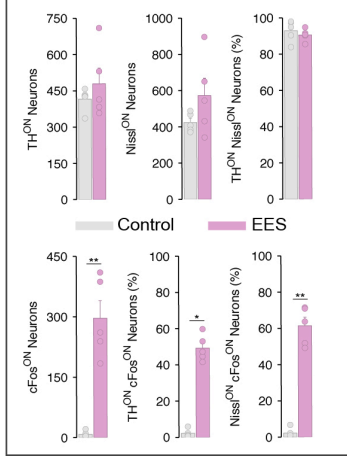
Step 1 (a)

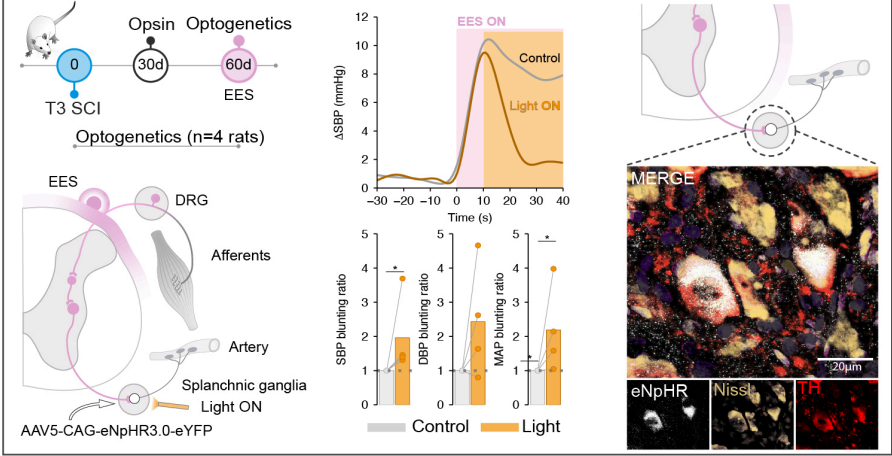Hemodynamic hotspot stimulation with EES results in activation of splanchnic ganglia neurons
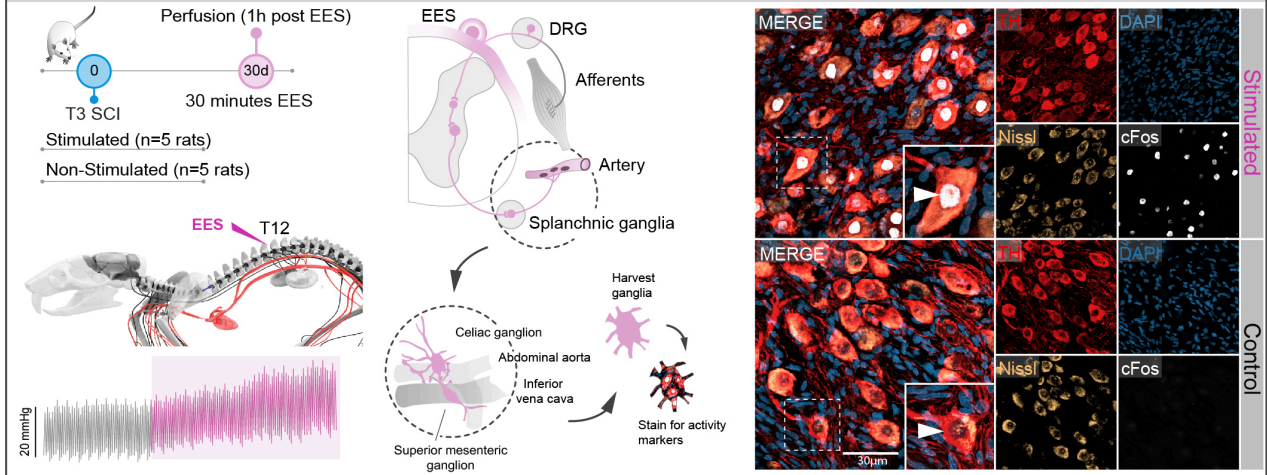
Step 2 (b)

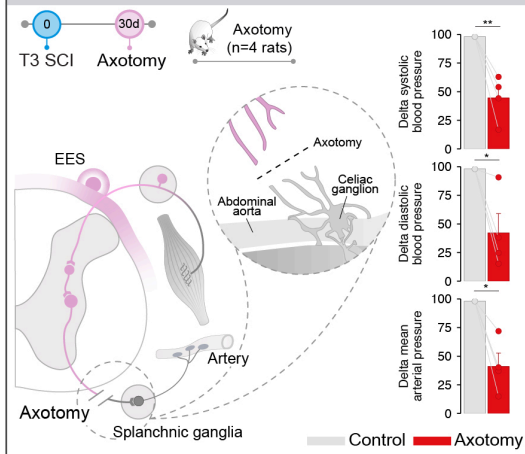Stimulation leads to an increased number of cFos positive neurons

Step 3 (c)

Optogenetic inhibition of ganglionic neurons results in blunting of pressor response elicited by EES
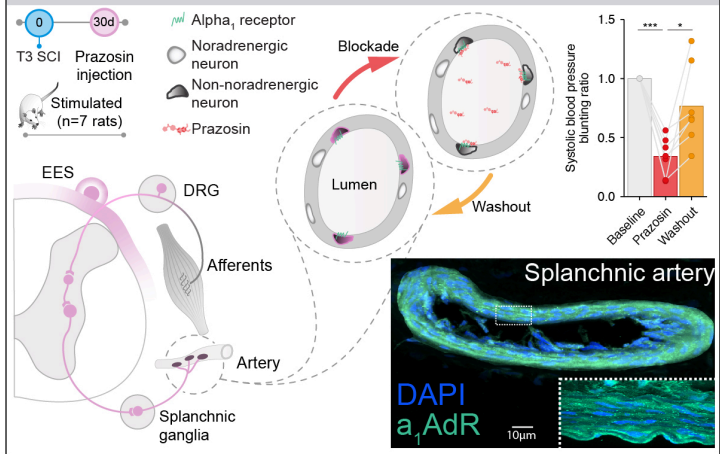
Step 4 (d)

Afferent nerve axotomy of ganglionic neurons results in loss of EES induced pressor response

Step 5 (e)

Alpha$_1$ receptor blockade blocks the effect of EES on blood pressure

Extended Data Figure 5. Epidural electrical stimulation induces pressor responses through the recruitment of splanchnic ganglia.

Step 1(a): To determine whether epidural electrical stimulation activated splanchnic ganglia we stimulated rats with T3 spinal cord injury (SCI) for thirty minutes (n = 5), or did not stimulate them (n = 5). We harvested the splanchnic ganglia and subjected them to immunohistochemisty. We stained each section for tyrosine hydroxylase (TH), cFos (immediate early gene), DAPI, and Nissl to confirm neuronal phenotypes. We then used an automatic cell segmentation algorithm to identify cells that coexpressed TH, Nissl, and or cFos.

Step 2(b): Quantifications revealed that animals stimulated with thirty minutes of EES had more cFos positive neurons than unstimulated rats (independent samples one-tailed t-test; t = 6.56; P = 0.001), and that these neurons colocalized with TH and Nissl stains (both p < 0.001).
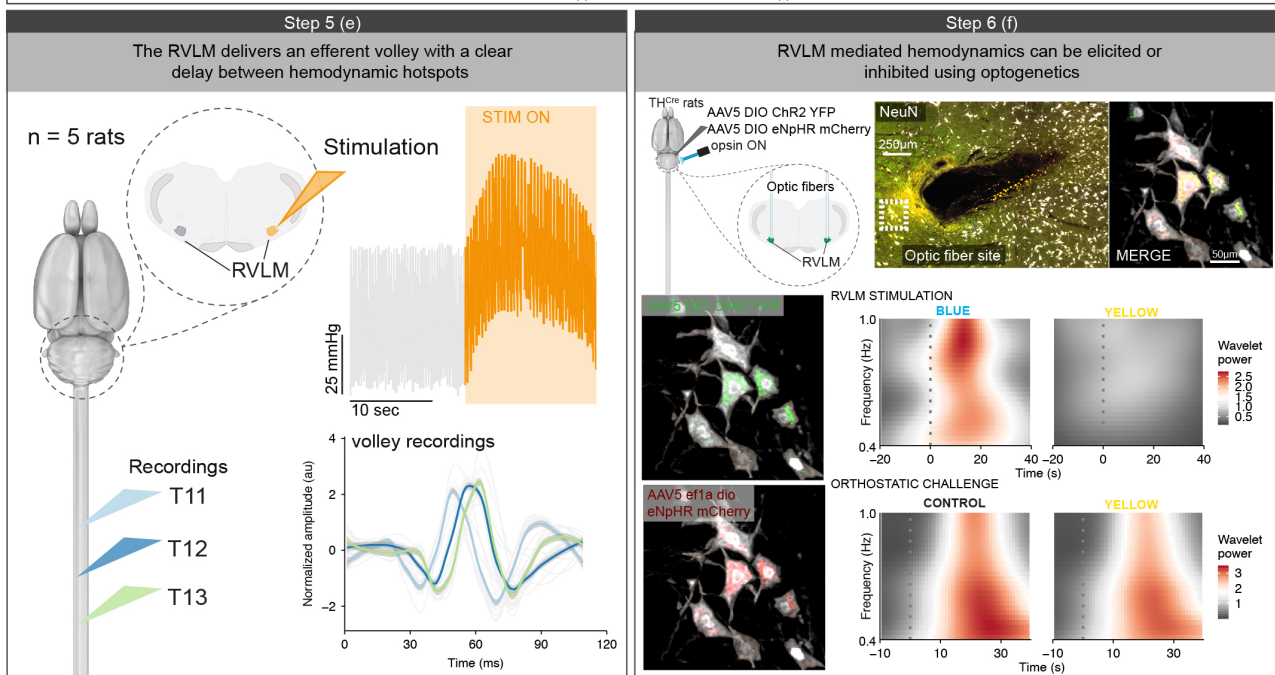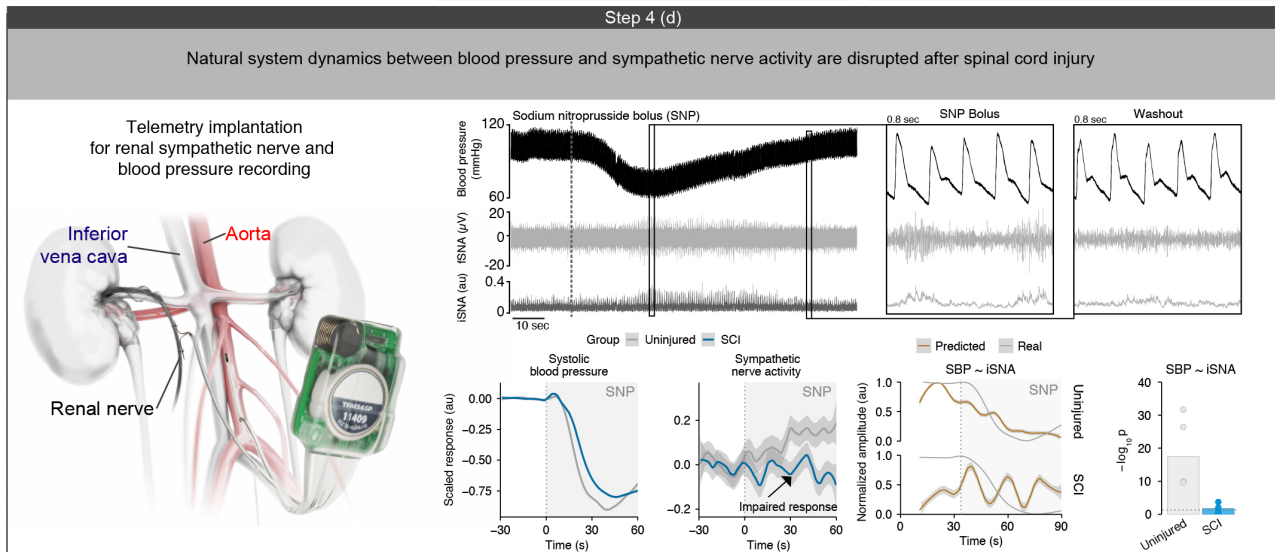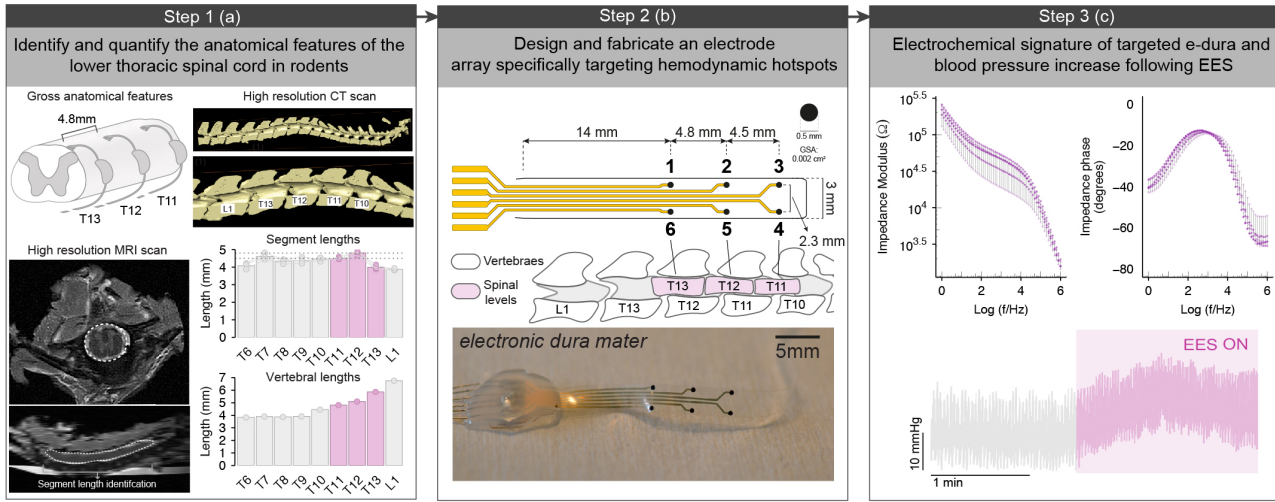
Step 3(c): We next completed two loss of function studies to examine the causal role of the splanchnic ganglia in the pressor responses to EES. We conducted an optogenetics silencing experiment (n = 4) and an axotomy experiment whereby we surgically severed the connection between the sympathetic pre-ganglionic neurons in the spinal cord and the splanchnic ganglia (n = 4). We completed these experiments on animals 60 days after T3 spinal cord injury. For optogenetics experiments viral injections occurred at 30 days post-injury. Activating the inhibitory opsin eNpHr3.0 with yellow light suppressed the pressor response to EES, and therefore increased the difference between the peak response to EES and the minimum response during light (or control) for systolic blood pressure (independent samples one-tailed t-test; 7 mmHg vs. 12 mmHg; t = 2.90; P = 0.031) and mean arterial pressure (independent samples one-tailed t-test; 7 mmHg vs. 13 mmHg; t = 2.60; P = 0.040).

Step 4(d): Axotomy of the connection between sympathetic pre-ganglionic neurons and splanchnic ganglia likewise blunted the pressor response for systolic blood pressure (n = 4; independent samples one-tailed t-test; 20 mmHg vs. 9.2 mmHg; t = -4.54; P = 0.001), diastolic blood pressure (independent samples one-tailed t-test; 19.6 mmHg vs. 7 mmHg; t = -2.40; P = 0.048), and mean arterial pressure (independent samples one-tailed t-test; 19 mmHg vs. 7 mmHg; t = -3.08; P = 0.027). These experiments indicate the splanchnic ganglia are necessary to induce a pressor response with EES.

Step 5(e): We next tested whether blocking alpha$_1$ receptors on systemic blood vessels would blunt the response to EES. We administered IV prazosin and found an immediate loss of pressor responses to EES (n = 7). The response returned after drug washout (one-way repeated measures ANOVA; 18 mmHg vs. 5.7 mmHg vs. 13.1 mmHg; F_2 = 15.63; P = 0.0001; Tukey HSD).

*P < 0.05; **P < 0.01; ***P < 0.001.

Abbreviations; DRG: dorsal root ganglia; SBP: systolic blood pressure; EES: targeted epidura spinal stimulation; TH: tyrosine hydroxylase.

Step 1 (a)

Identify and quantify the anatomical features of the lower thoracic spinal cord in rodents

Step 2 (b)

Design and fabricate an electrode array specifically targeting hemodynamic hotspots

Step 3 (c)

Electrochemical signature of targeted e-dura and blood pressure increase following EES

Step 4 (d)

Natural system dynamics between blood pressure and sympathetic nerve activity are disrupted after spinal cord injury

Step 5 (e)

The RVLM delivers an efferent volley with a clear delay between hemodynamic hotspots

Step 6 (f)

RVLM mediated hemodynamics can be elicited or inhibited using optogenetics

Extended Figure 6. Mechanistic insight enabled the development of a targeted electronic dura mater and biomimetic stimulation strategy to recapitulate the natural dynamics of the sympathetic nervous system.

Step 1(a): To develop the spatial features of an electrode array specifically targeting hemodynamic hotspots we first quantified all the features of the low thoracic spinal column. We measured the precise length of each spinal segment and vertebrae using a combination of gross anatomical dissections, high resolution CT scans, and custom MRI sequences.

Step 2(b): We used these anatomical features, driven by the identification of *hemodynamic hotspots* to develop an electronic dura mater specifically targeting T11, T12, and T13 spinal segments. Detailed dimensions of the active stimulation sites (500 μm diameter, 0.002 cm^2 geometric surface area).

Step 3(c): When placed on the spinal cord, the array increases blood pressure and all electrodes are functional. Top: electrochemical impedance spectrum (modulus, left and phase, right) of an electrode array acquired *in vitro* post-fabrication.
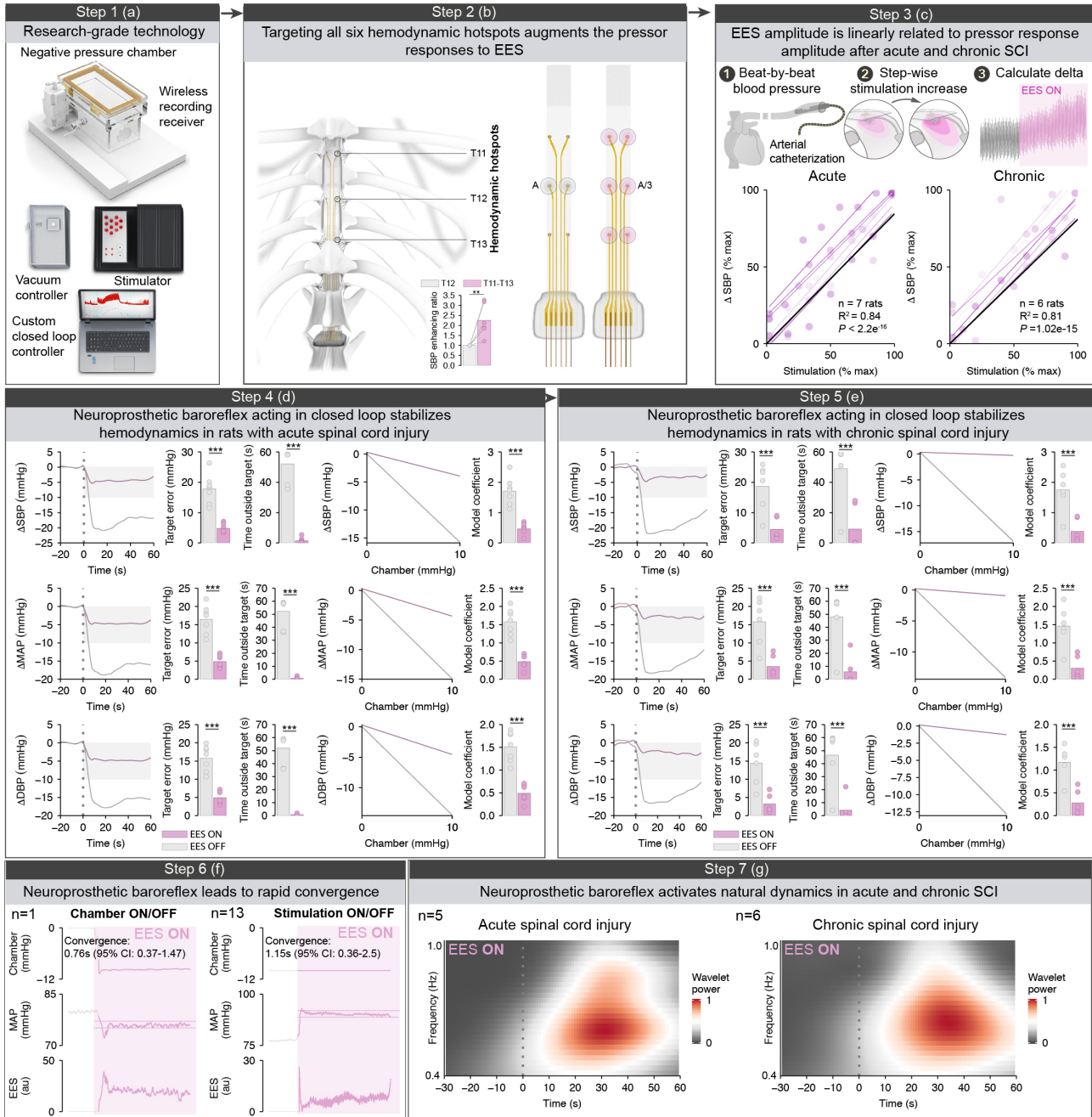
Step 4(d): To recapitulate the natural dynamics of the sympathetic nervous system we first recorded neural activity from the renal sympathetic nerve and blood pressure from the descending aorta. We measured these signals in response to a hypotensive stimulus (sodium nitroprusside [SNP]) in both injured and uninjured animals (n = 5; uninjured example shown). We found that there was an impaired response in the sympathetic nerve activity after SCI. To quantify the changes in these dynamics we trained a feed-forward neural network to predict a continuous output from a given input. For example, predicting systolic blood pressure from sympathetic nerve activity (iSNA) (i.e., SBP ~ iSNA). We found that in uninjured animals there were strong correlations whereby the model could predict one from the other. In injured animals this correlation was absent. Here, we show the ability of the model to predict SBP from iSNA in response to this stimulus (strength of correlation [Pearson correlation] presented as -log$_{10}$(p) for each group). Responses are presented on a normalized delta scale to account for absolute differences between animals.

Step 5(e): To understand the timing delay of RVLM activation to sympathetic outflow from the spinal cord we stimulated the RVLM electrically, and measured the efferent volley over T11, T12, and T13 (n = 5). Stimulation of the RVLM dramatically increased blood pressure, confirming localization of the stimulation. We then measured the delay between action potentials in response to 100Hz 10s pulse trains of RVLM stimulation and found a 2.5 ± 0.4ms delay between segments. Representative traces across segments are shown for one animal. We therefore integrated this delay into the stimulation design between segments.

Step 6 (f): Finally, to understand the precise role of frequency dynamics in blood pressure control we stimulated the RVLM using optogenetics in TH-Cre rats. We found that stimulation with blue light led to a robust increase in wavelet spectrogram within the 0.4-1.0Hz band (paired samples one-tailed t-test; t = 2.67; *P* = 0.028). This was in contrast to activation of an inhibitory opsin using a yellow laser (which would, in this case, inhibit the RVLM due to the presence of an inhibitory opsin), which showed significantly less activation compared to blue light (paired samples one-tailed t-test; t = 2.44; *P* = 0.035). In response to an orthostatic challenge, the wavelet power response in uninjured rats was less pronounced in the presence of inhibitory (yellow) light (bottom panels; independent samples one-tailed t-test; t = 4.04; *P* = 0.008).

P < 0.05; **P* < 0.01; ***P* < 0.001.

Abbreviations: iSNA: integrated sympathetic nerve activity; RVLM: rostral ventrolateral medulla; SBP: systolic blood pressure; EES: targeted epidural spinal stimulation; TH: tyrosine hydroxylase.

Step 1 (a)
Research-grade technology

Negative pressure chamber

Wireless recording receiver

Vacuum controller

Stimulator

Custom closed loop controller

Step 2 (b)
Targeting all six hemodynamic hotspots augments the pressor responses to EES

T11
T12
T13

Hemodynamic hotspots

A   A/3

SBP enhancing ratio
3.5
3.0
2.5
2.0
1.5
1.0
0.5
0.0

T12   T11-T13
**

Step 3 (c)
EES amplitude is linearly related to pressor response amplitude after acute and chronic SCI

1 Beat-by-beat blood pressure
2 Step-wise stimulation increase
3 Calculate delta

EES ON

Arterial catheterization

Acute

Δ SBP (% max)
100

50

0
0   50   100
Stimulation (% max)

n = 7 rats
R^2 = 0.84
$P < 2.2e^{-16}$

Chronic

Δ SBP (% max)
100

50

0
0   50   100
Stimulation (% max)

n = 6 rats
R^2 = 0.81
$P = 1.02e^{-15}$

Step 4 (d)
Neuroprosthetic baroreflex acting in closed loop stabilizes hemodynamics in rats with acute spinal cord injury

ΔSBP (mmHg)
Target error (mmHg) ***
Time outside target (s) ***
ΔSBP (mmHg)
Model coefficient ***

ΔMAP (mmHg)
Target error (mmHg) ***
Time outside target (s) ***
ΔMAP (mmHg)
Model coefficient ***

ΔDBP (mmHg)
Target error (mmHg) ***
Time outside target (s) ***
ΔDBP (mmHg)
Model coefficient ***

EES ON
EES OFF

Time (s)
Chamber (mmHg)

Step 5 (e)
Neuroprosthetic baroreflex acting in closed loop stabilizes hemodynamics in rats with chronic spinal cord injury

ΔSBP (mmHg)
Target error (mmHg) ***
Time outside target (s) ***
ΔSBP (mmHg)
Model coefficient ***

ΔMAP (mmHg)
Target error (mmHg) ***
Time outside target (s) ***
ΔMAP (mmHg)
Model coefficient ***

ΔDBP (mmHg)
Target error (mmHg) ***
Time outside target (s) ***
ΔDBP (mmHg)
Model coefficient ***

EES ON
EES OFF

Time (s)
Chamber (mmHg)

Step 6 (f)
Neuroprosthetic baroreflex leads to rapid convergence

n=1   **Chamber ON/OFF**
EES ON
Convergence: 0.76s (95% CI: 0.37-1.47)

Chamber (mmHg)
MAP (mmHg)
EES (au)

n=13   **Stimulation ON/OFF**
EES ON
Convergence: 1.15s (95% CI: 0.36-2.5)

Chamber (mmHg)
MAP (mmHg)
EES (au)

Step 7 (g)
Neuroprosthetic baroreflex activates natural dynamics in acute and chronic SCI

n=5   Acute spinal cord injury

EES ON

Frequency (Hz)
1.0

0.4
-30 -20 -10 0 10 20 30 40 50 60
Time (s)

Wavelet power
1
0

n=6   Chronic spinal cord injury

EES ON

Frequency (Hz)
1.0

0.4
-30 -20 -10 0 10 20 30 40 50 60
Time (s)

Wavelet power
1
0

29

Extended Data Figure 7. Neuroprosthetic baroreflex implemented in rodents with SCI.

Step 1(a): We tested whether we could stabilize hemodynamics using the *neuroprosthetic baroreflex*, operating in closed-loop, in animals with acute (*n* = 7; 12 hours post-injury) and chronic (*n* = 6; one month post-injury) T3 spinal cord injury (SCI). We implemented the *neuroprosthetic baroreflex* within research-grade technology in order to achieve precise control over stimulation parameters.

Step 2(b): Schematic of electronic dura mater electrode arrays targeting hemodynamic hotspots. Barplot reports relative pressor responses (SBP: systolic blood pressure; n = 5, independent samples one-tailed t-test; t = 3.90; *P* = 0.006).

Step 3(c): We found a linear relationship between stimulation amplitude and the pressor response to stimulation in both animals with acute (mixed model linear regression; R2 = 0.84, P < $2.2e^{-16}$) and chronic (mixed model linear regression; R2 = 0.81, *P* < $1.0e^{-15}$) spinal cord injury.

Step 4(d): We completed a series of trials to test the ability of the *neuroprosthetic baroreflex* to stabilize hemodynamics in rats with acute spinal cord injury. The *neuroprosthetic baroreflex* was activated in closed-loop prior to the activation of the lower-body negative pressure chamber. In trials where the stimulation was ON, we found a reduction in the target (baseline) error (paired samples one-tailed t-tests; SBP: t = -6.12, *P* = $5.50e^{-04}$; MAP; t = -6.08, *P* = $4.48e^{-04}$; DBP; t = -5.85, *P* = $4.34e^{-04}$) reduced time outside key thresholds (-10 mmHg; paired samples one-tailed t-tests; SBP: t = -12.52, *P* = $9.94e^{-06}$; MAP; t = -12.29, *P* = $8.83e^{-06}$; DBP; t = -11.73, *P* = $1.15e^{-05}$), a restoration of the non-linear relationship between blood pressure and chamber pressure, and a concomitant reduction in the linear model coefficient (likelihood ratio test of nested models; all *P* < 0.001). These quantifications held for systolic blood pressure (top), diastolic blood pressure (middle), and mean arterial pressure (bottom).
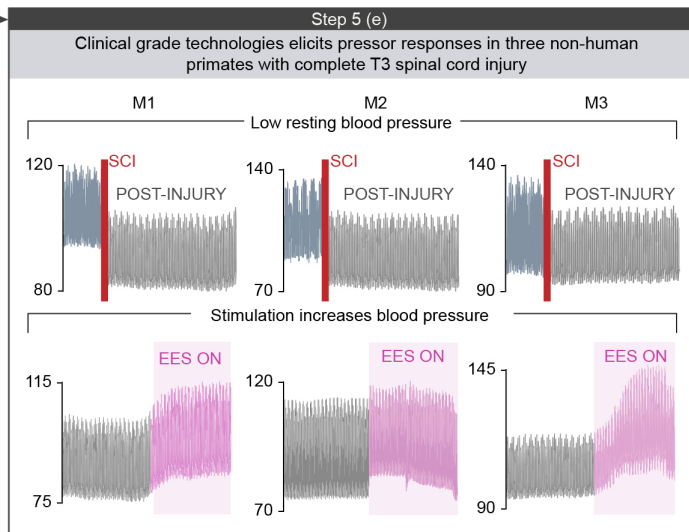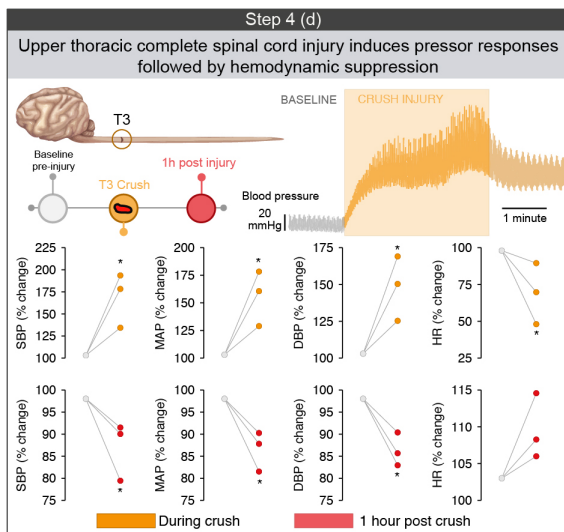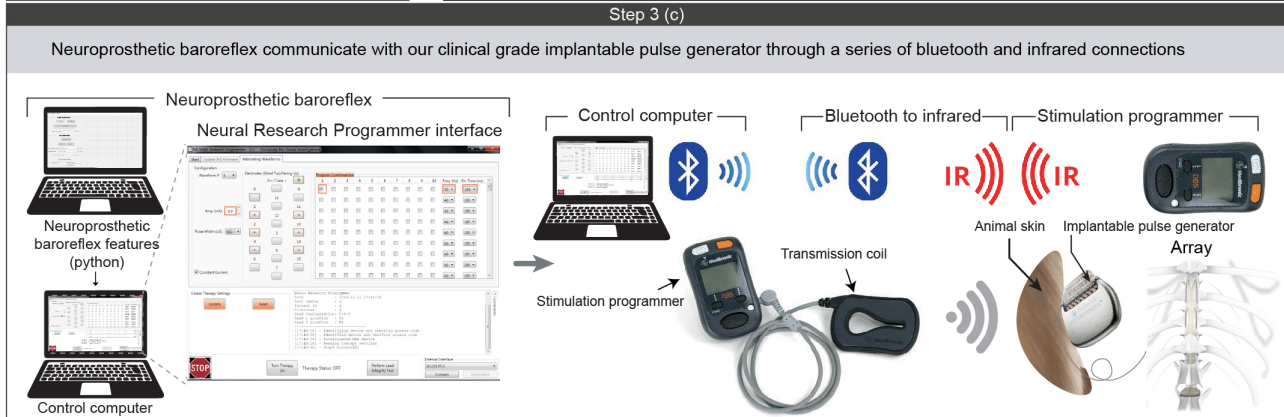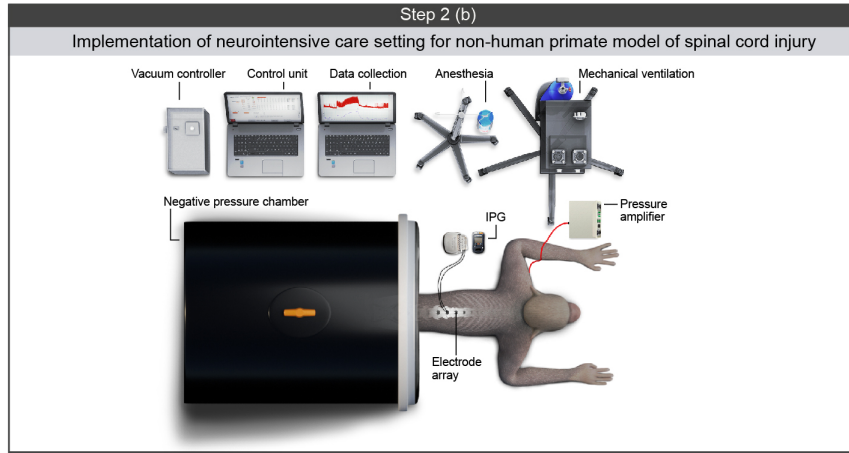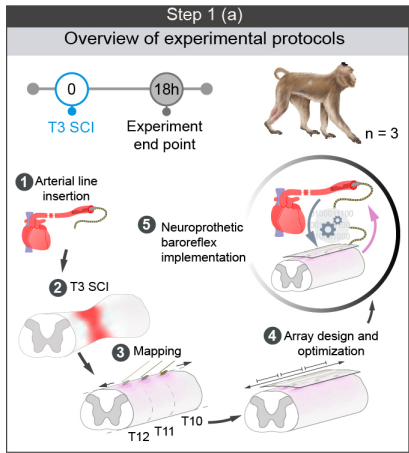
Step 5(e): We completed the exact same experiments on animals with chronic spinal cord injury and found similar results to those of the acutely injured rats. Specifically, in trials where the stimulation was ON, we found a reduction in the target (baseline) error (paired samples one-tailed t-tests; SBP: t = -3.84, *P* = 0.006; MAP; t = -3.83, *P* = 0.006; DBP; t = -3.83, *P* = 0.006), reduced time outside key thresholds (-10 mmHg; paired samples one-tailed t-tests; SBP: t = -4.37, *P* =0.004; MAP; t = -4.43, *P* = 0.003; DBP; t = -4.21, *P* = 0.004), a restoration of the non-linear relationship between blood pressure and chamber pressure, and a concomitant reduction in the linear model coefficient (likelihood ratio test of nested models; all *P* < 0.001). These quantifications held for systolic blood pressure (top), diastolic blood pressure (middle), and mean arterial pressure (bottom).

Step 6(f): We found that in response to stimulation blood pressure rapidly reached the set-point, with convergence times of 0.76s in the example case presented in **Figure 3**, and 1.15s (95% CI: 0.36 – 2.5s) across n = 13 animals in response to the negative pressure chamber. In this case convergence was defined as stable within 2.5 mmHg.

Step 7(g): The neuroprosthetic baroreflex, acting in closed loop, re-established natural frequency dynamics (increased wavelet power in the 0.4-1.0Hz spectrogram) in both animals with acute (paired samples one-tailed t-test; t = 4.46; *P* = 0.002) and chronic SCI (paired samples one-tailed t-test; t = 3.37; *P* = 0.014). *P* < 0.05; **P* < 0.01; ***P* < 0.001.

Abbreviations: DBP: diastolic blood pressure; MAP: mean arterial pressure; RVLM: rostral ventrolateral medulla; SBP: systolic blood pressure; SBP: systolic blood pressure; SCI: spinal cord injury; EES: targeted epidural spinal stimulation.

Step 1 (a)
Overview of experimental protocols

T3 SCI — 0 — Experiment end point — 18h

n = 3

1. Arterial line insertion
2. T3 SCI
3. Mapping
4. Array design and optimization
5. Neuroprosthetic baroreflex implementation

T12 T11 T10

Step 2 (b)
Implementation of neurointensive care setting for non-human primate model of spinal cord injury

Vacuum controller | Control unit | Data collection | Anesthesia | Mechanical ventilation

Negative pressure chamber

IPG | Pressure amplifier

Electrode array

Step 3 (c)
Neuroprosthetic baroreflex communicate with our clinical grade implantable pulse generator through a series of bluetooth and infrared connections

Neuroprosthetic baroreflex

Neural Research Programmer interface

Neuroprosthetic baroreflex features (python)

Control computer

Control computer

Bluetooth to infrared

Stimulation programmer

Transmission coil

Stimulation programmer

Animal skin | Implantable pulse generator

Array

Step 4 (d)
Upper thoracic complete spinal cord injury induces pressor responses followed by hemodynamic suppression

T3

Baseline pre-injury — T3 Crush — 1h post injury

BASELINE | CRUSH INJURY

Blood pressure 20 mmHg

1 minute

SBP (% change), MAP (% change), DBP (% change), HR (% change)

During crush | 1 hour post crush

Step 5 (e)
Clinical grade technologies elicits pressor responses in three non-human primates with complete T3 spinal cord injury

M1 | M2 | M3

Low resting blood pressure

SCI POST-INJURY

Stimulation increases blood pressure

EES ON

Extended Data Figure 8. Translation of the neuroprosthetic baroreflex to non-human primates.

Step 1(a): To further establish the efficacy of the *neuroprosthetic baroreflex* we performed experiments in three non-human primates. First, we measured arterial blood pressure using an invasive catheter in the subclavian artery. Next, we performed a T3 spinal cord injury (SCI) in order to mimic the experimental conditions of our rodent experiments. We next mapped the pressor responses to epidural stimulation from T7 to L3. We combined these results with *ex-vivo* dissections of the anatomical dimensions of the lower thoracic spinal cord in Rhesus Macaques (*n* = 3) to design an electronic dura mater. Finally, we implemented all the features of the *neuroprosthetic* baroreflex.

Step 2(b): We tested the efficacy of the *neuroprosthetic baroreflex* specifically within the context of acute traumatic SCI. We emulated all the features of standard neurointensive care including arterial blood pressure measurements, clinical grade anesthesia (intravenous Propofol), as well as temperature and respiration control. We integrated our stimulation approach into clinical-grade technologies using an implantable pulse generator and a spatially selective spinal implant.

Step 3(c): All the features of the *neuroprosthetic baroreflex* were injected into our previously used clinical-grade stimulation approach. Briefly, the *neuroprosthetic baroreflex* received beat-by-beat continuous blood pressure in order to provide closed loop control. Stimulation output control was sent to the neural research programmer interface, which communicates with the implantable pulse generator through a series of bluetooth and infrared links. These commands were then sent directly to the customized spinal implant.

Step 4(d): Similar to rodent experiments, we found that T3 spinal cord injury induced a significant surge in systolic blood pressure (paired one-tailed t-test; 127 mmHg vs. 213 mmHg; t = 4.15; *P* = 0.027), mean arterial pressure (paired one-tailed t-test; 110 mmHg vs. 172 mmHg; t = 3.96; *P* = 0.029), diastolic blood pressure (paired one-tailed t-test; 102 mmHg; vs. 151 mmHg; t = 3.80; *P* = 0.031), and an accompanying decrease in heart rate (paired one-tailed t-test; 111 bpm vs. 76 bpm; t = -4.05; *P* = 0.028). By one-hour post-injury we observed clinically relevant neurogenic shock, characterized by decreased systolic blood pressure (paired one-tailed t-test; 127 mmHg vs. 110 mmHg; t = -3.20; *P* = 0.043), mean arterial pressure (paired one-tailed t-test; 110 mmHg vs. 95 mmHg; t = -5.23; *P* = 0.017), and diastolic blood pressure (paired one-tailed t-test; 96 mmHg vs. 102 mmHg; t = -6.24; *P* = 0.012).

Step 5(e): Despite the fact that we observed an immediate decrease in resting blood pressure, epidural electrical stimulation was able to cause an immediate and transient pressor response in all three animals. In all cases, where percent change is presented statistics were completed on raw values.

*P < 0.05; ***P* < 0.01; ****P* < 0.001.

Abbreviations: DBP: diastolic blood pressure; EES: targeted epidural spinal stimulation HR: heart rate; MAP: mean arterial pressure; SBP: systolic blood pressure; SCI: spinal cord injury.

Step 1 (a)
Functional mapping reveals conserved hemodynamic hotspots in non-human primates

① Arterial catheterization
② Mapping
③ Calculate delta

EES

Systolic blood pressure · Mean arterial pressure · Diastolic blood pressure

Normalized TESS response

T7 T8 T9 T10 T11 T12 L1 L3

Step 2 (b)
Neuroanatomical substrate is conserved across species

Rat   Monkey

T7 T8 T9 T10 T11 T12 T13 L1

Rat response (au)
T9/T10 T7/T8 T10/T11 T12/T13 T11/T12 T8/T9 L1/L1

NHP response (au)

Step 3 (c)
Anatomical features of the lower thoracic spine and spinal cord are precisely quantified

ev-vivo dissections (n = 3)   5 cm
T12 T10 T8 T6 T4
T11 T9 T7 T5

High resolution MRI
Spinal cord
Posterior roots

Segment Length (cm)
T8 T9 T10 T11 T12 L1

Step 4 (d)
Soft electrode array is designed to specifically target hemodynamic hotspots

15.1 mm   15.2 mm   15.5 mm
2 mm
0.7 mm
GSA: 0.014 cm²
1   2   3
6 mm   8 mm
6   5   4

Step 5 (e)
Electrochemical signature of e-dura soft electrode array

Electrode impedence

Impedance Modulus (Ω)
Log (f/Hz)

Impedance phase (degrees)
Log (f/Hz)

Step 6 (f)
Implementation of negative pressure chamber in non-human primates

Chamber **ON**
Delta Systolic Blood Pressure (mmHg)
Negative pressure chamber

Chamber pressure (mmHg)
Time (s)

Step 7 (g)
Hemodynamics respond linearly to increasing stimulation amplitude. Stimulation of three hemodynamic hotspots is superior to one hotspot

Step-wise stimulation increase

Single segment stimulation versus whole array
T11 A A/3 A/3 T10 A/3 T11 T12

n = 3 monkeys
R² = 0.85
p = 9.33e-09

Max Change SBP (%)
Stimulation (% max)

Systolic blood pressure · Mean arterial pressure · Diastolic blood pressure

Max Change (%)
T11   ARRAY

Step 8 (h)
Closed loop biomimetic stimulation stabilizes hemodynamics without fatigue and restores natural system dynamics

Biomimetic stimulation

Continuous stimulation fails to maintain pressor response

n = 1 monkey
Continuous
Biomimetic
ΔSBP (mmHg)
Time (s)

Biomimetic stimulation reinstates natural dynamics

Continuous stimulation

Continuous stimulation   Biomimetic stimulation
Frequency (Hz)
Wavelet power
Time (s)

Step 9 (i)
Neuroprosthetic baroreflex stabilizes hemodynamics after acute spinal cord injury

n = 2 monkeys
ΔSBP (mmHg)   Target error (s)   Time outside target (s)   ΔSBP (mmHg)   Model coefficient
Time (s)   Chamber (mmHg)

ΔMAP (mmHg)   Target error (mmHg)   Time outside target (s)   ΔMAP (mmHg)   Model coefficient
Time (s)   Chamber (mmHg)

ΔDBP (mmHg)   Target error (mmHg)   Time outside target (s)   ΔDBP (mmHg)   Model coefficient
Time (s)   Chamber (mmHg)

EES OFF   EES ON

Extended Data Figure 9. Neuroprosthetic baroreflex implemented in non-human primates with spinal cord injury.

Step 1(a): We recorded blood pressure using an axillary artery catheterization preparation, and calculated the peak change in blood pressure during stimulation. We found that there was a *hemodynamic hotspot* in the lower thoracic spinal cord, specifically over segments T10, T11, and T12.

Step 2(b): Accounting for the offset in segments between species, we found a linear relationship between the functional mapping results in rats and the functional mapping results in non-human primates, further confirming the localization of a *hemodynamic hotspot* in the last three thoracic segments (linear modelling; R^2 = 0.65; *P* = 0.018).

Step 3(c): To develop the spatial features of an electrode array specifically targeting *hemodynamic hotspots* in the non-human primate we quantified all the features of the low thoracic spinal column. We measured the precise length of each spinal segment and vertebra using a combination of gross anatomical dissections, high resolution CT scans, and custom MRI sequences.

Step 4(d): We used these anatomical features, driven by the identification of hemodynamic hotspots to develop an electronic dura mater specifically targeting T10, T11, and T12 spinal segments. Detailed dimensions of the active stimulation sites (0.7 mm diameter, 0.014 cm^2 geometric surface area).

Step 5(e): Electrochemical impedance spectrum (modulus, left and phase, right) of an electrode array acquired *in vitro* post-fabrication indicates functional, low-impedance electrodes.

Step 6(f): We fully implemented a negative pressure chamber designed to fit a non-human primate in order to induce a stimulated orthostatic challenge. We found that stimulation using the chamber led to an immediate and consistent decrease in blood pressure.

Step 7(g): We next implemented our biomimetic stimulation protocols. We found a linear relationship between stimulation amplitude and the pressor response (n = 3 monkeys; linear modelling, R2 = 0.85; *P* = 9.33e^{-05}). Compared to stimulating only one hotspot, stimulating with all three sets of electrodes, and therefore targeting each *hemodynamic hotspot* led to a more robust increase in blood pressure (n = 2 monkeys).

Step 8(h): Implementation of the *neuroprosthetic baroreflex*, acting in closed loop, led to sustained increases in blood pressure that did not fatigue (n = 1 monkey). In comparison, continuous open-loop stimulation, using the same stimulation parameters, elicited an increase in blood pressure that was immediately followed by rapid fatigue. For continuous stimulation, the amplitude was set to the maximum observed stimulation value in the trials with the closed-loop controller. Only biomimetic stimulation re-established the natural frequency dynamics, revealed using wavelet decomposition (n = 2 monkeys).

Step 9(i): Using this closed loop approach, we found a reduction in the target (baseline) error, reduced time outside key thresholds (-5 mmHg; -2 mmHg for diastolic blood pressure), a restoration of the non-linear relationship between blood pressure and chamber pressure, and a concomitant reduction in the linear model coefficient. These quantifications held for systolic blood pressure (top), diastolic blood pressure (middle), and mean arterial pressure (bottom).

Abbreviations: DBP: diastolic blood pressure; MAP: mean arterial pressure; SBP: systolic blood pressure; EES: targeted epidural spinal stimulation.
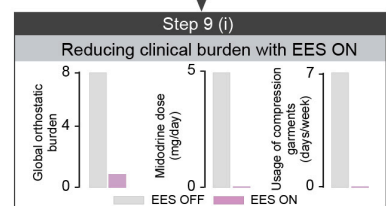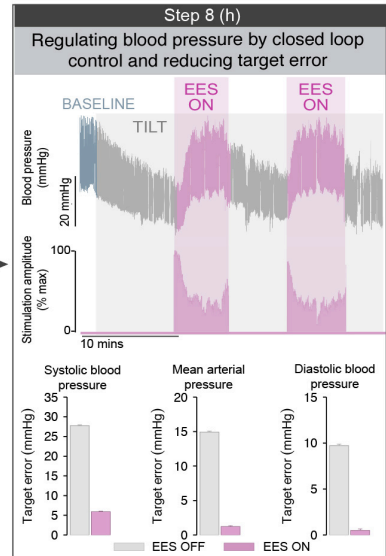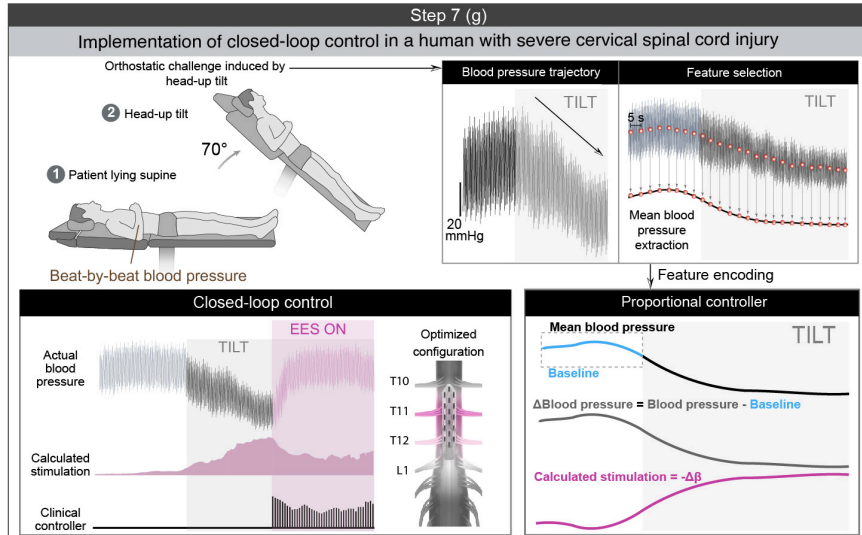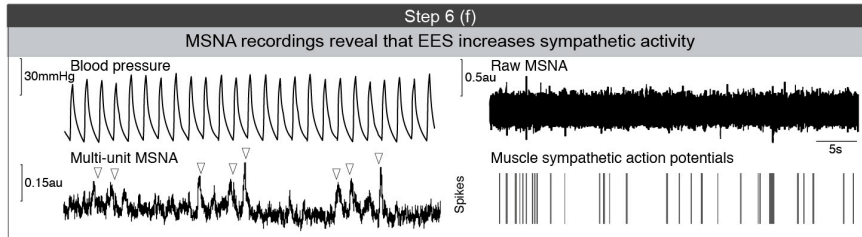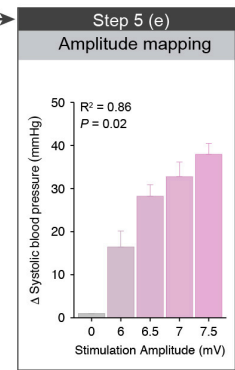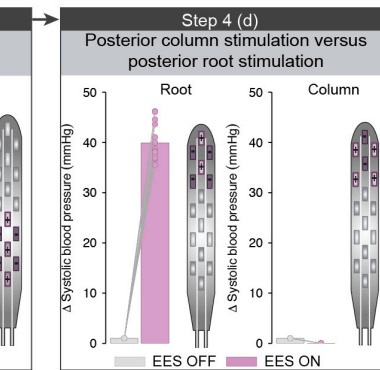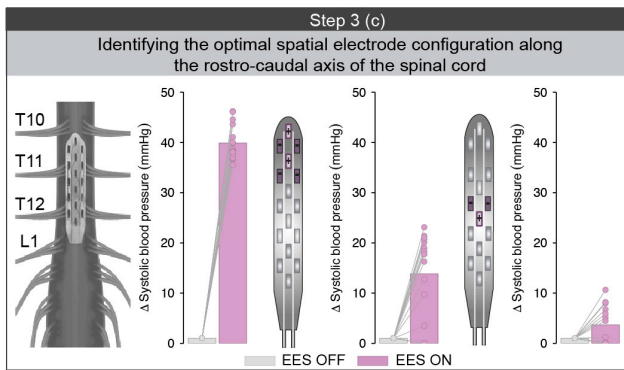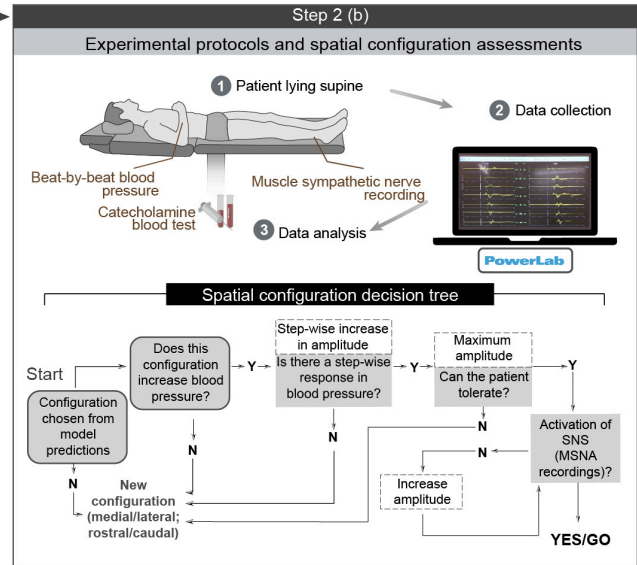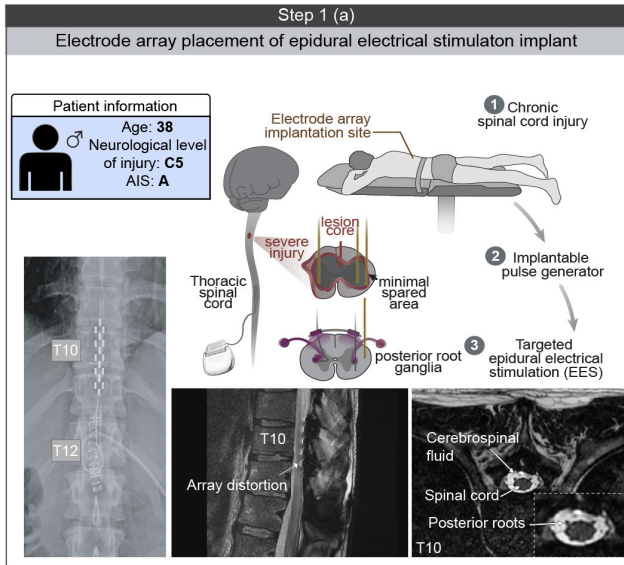
Extended Data Figure 10. Targeted epidural electrical stimulation enables control of hemodynamics in a human with spinal cord injury.

Step 1(a): We implanted a 5-6-5 Medtronic paddle array below the T10 and T11 vertebral bodies in a 38-year-old patient with clinically-complete cervical spinal cord injury (SCI) presenting with medically-refractory orthostatic hypotension. We confirmed the paddle array location with computerized tomography and magnetic resonance imaging.

Step 2(b): We recorded hemodynamics, muscle sympathetic nerve activity and catecholamine levels in the patient without and with stimulation. We used personalized computational modelling and a genetic algorithm to predict the ideal spatial configurations to activate the lower thoracic spinal segments. We then used the illustrated decision-making process to determine whether to move forward with the use of a given configuration.

Step 3(c): We identified an optimal configuration, which recruited the lower thoracic spinal segments, increased blood pressure, normalized plasma norepinephrine levels, and increased muscle sympathetic nerve activity. We tested other configurations that are not optimally targeted to these roots and found the blood pressure responses were not robust.

Step 4(d): Activation of the posterior columns using medial electrodes did not lead to a pressor response.

Step 5(e): Using the optimal configuration, we found a stepwise increase in blood pressure as we increased the amplitude of stimulation (R^2 = 0.86; P = 0.02; linear regression). Data are mean ± SEM.

Step 6(f): Blood pressure and muscle sympathetic nerve activity (MSNA) recordings during EES. The top left panel shows the blood pressure recording and the bottom left panel shows the rectified and integrated (mean voltage) neurogram demonstrating multi-unit MSNA. Triangles identify the accepted multi-unit MSNA bursts (broad base width with a peak surpassing 3 times the noise width). The mean voltage neurogram is derived from the raw MSNA neurogram in the top right panel, which is the amplified and bandpass filtered neurogram. The bottom right tracing shows the MSNA action potential spike events over time that were derived from the raw MSNA neurogram above.

Step 7(g): To test whether the concept of the neuroprosthetic baroreflex could be implemented in humans, we verticalized the patient to induce an orthostatic challenge while recording blood pressure. We performed feature extraction to obtain a rolling mean blood pressure, from which we calculated a continuous error (delta blood pressure). We then adjusted the weighted proportion to generate a calculated stimulation output, which was implemented using a clinician controller to modulate blood pressure in closed-loop.

Step 8(h): When our closed-loop system was activated, blood pressure was tightly regulated evidenced by stabilized blood pressure and mitigated target error.

Step 9(i): This patient now uses the stimulation daily and has been able to cease other treatments for orthostatic hypotension. Furthermore, the daily use of this therapy has reduced the self-reported burden of orthostatic hypotension for this patient, as assessed using clinical questionnaires.

Abbreviations: AIS: American spinal injury association impairment scale; MSNA: muscle sympathetic nerve activity; EES: targeted epidural spinal stimulation.

ONLINE METHODS

Animal models
Experiments were conducted on adult female Lewis rats (180–220 g body weight, 14–30 weeks of age) and adult male or female TH-Cre rats (180–400 g body weight, 14–30 weeks of age) [27]. Housing, surgery, behavioral experiments and euthanasia were performed in compliance with the Swiss Veterinary Law guidelines. Animal care, including manual bladder voiding, was performed twice daily for the first 2 weeks after injury and once daily for the remaining post-injury period[45]. Procedures and surgeries were approved by the Veterinary Office of the Canton of Geneva (Switzerland; GE/87/17 and GE/212/17) and the University of Calgary (AC17-0185). Non-human primate experiments were approved by the Institutional Animal Care and Use Committee of China Academy of Medical Sciences in Beijing (LQ19003) and performed in accordance with the European Union directive of 22 September 2010 (2010/63/EU) on the protection of animals used for scientific purposes in an AAALAC-accredited facility (Chinese Academy of Science, Beijing, China), as we have previously described[11]. Three healthy male Rhesus monkeys (Macaca mulatta) aged 5 years old, and weighing 5.4, 5.4 and 5.8 kg were housed individually in cages designed according to European guidelines (2 m × 1.6 m × 1.26 m). Environmental enrichment included toys and soothing music.

Rodent anesthesia use
All non-terminal experiments were conducted by anesthetizing animals with isoflurane (initial induction 5% and maintained on a Bain's system at 2%). Terminal electrophysiological assessments were carried out as previously described[46] four weeks after SCI. In brief, animals were anaesthetized with urethane (1.5 g/kg; intraperitoneally) and core body temperature was maintained at 37 °C using a self-regulating heated pad connected to a rectal probe. Depth of anaesthesia was continually monitored by assessing withdrawal reflexes and respiratory rate.

Surgical procedures and post-surgical care
Spinal cord injuries
Rodent spinal cord injuries were performed according to our previously published work[47,48]. Briefly, a laminectomy was performed on the TIII vertebra to expose the T3 spinal segment. Following this the animal was transferred to the Infinite-Horizons (IH-0400 Impactor, Precision Systems and Instrumentation LLC, USA) impactor[49] stage, where the TII and TIV spinous processes were securely clamped using modified Allis forceps[47]. The animal was stabilized on the platform and the impactor tip (2.5 mm) was properly aligned using a 3-dimensional coordinate system moving platform. The IH system was set to deliver an impact force of 400 kdyn, with a 5 second dwell time[47]. Analgesia (buprenorphine, Essex Chemie AG, Switzerland, 0.01–0.05 mg per kg, s.c.) and antibiotics (Amoxicillin 200mg/4ml Sandoz, Germany, 200mg/L *ad libitum*) were provided for 3 and 5 days after surgery, respectively. Bladders were manually expressed for approximately one week, after which time animals regained reflexive voiding[45,47].

For non-human primate experiments, all the surgical procedures were terminal. Animals were fasted for 12 hours prior to anesthesia to minimize the risk of vomiting and aspiration. Animals were first aseptically prepared and anesthetized with ketamine (10 mg/kg, intramuscular injection) and Propofol (6mg/kg loading followed by maintenance at 0.3mg/kg/min via an IV line). Animals were then intubated and put the tested animal on the surgery table. Ketamine and propofol will be complemented with isoflurane (1-3%). Hydration was maintained through IV fluids

at 5-10ml/kg/h. Temperature was maintained using heating blankets and a warmed table. A certified functional neurosurgeon (J.B.) supervised all the surgical procedures. The complete experiment for each animal was performed during a single operation lasting less than 12h. All three animals received a spinal cord injury. A partial laminectomy was made at the level of the T2/T3 thoracic vertebrae. The spinal cord was compressed for thirty seconds and then transected at the T3 segment. At the end-point of the experiment animals were further anesthetized (already in the surgical plane of anesthesia from the prior procedure) with an IM injection of Ketamine (15mg/kg) followed by IV Pentobarbital (100-150mg/kg) until cessation of breathing.

Epidural electrical stimulation implants
For positioning epidural stimulation electrodes in rats, targeted epidural spinal stimulation (EES) was delivered in three modes, as we have previously described[18,21,34,48,50]: 1) using a stereotax for functional mapping experiments, 2) with electrodes sewn to the dura[18,21,48,50], and 3) using e-dura technology[34]. For functional mapping, a Teflon-coated stainless-steel wire (AS632, Cooner Wire, USA) was fixed to a stereotax to allow stable placement of the electrode while mapping all spinal segments. Laminectomies were performed starting at L2, and moving rostral. Stimulation was provided at 50Hz, with a pulse length of 2ms, and the current increased from 0 to approximately 200mA. Upon visible motor threshold, the stimulation was stopped. For terminal experiments targeting *hemodynamic hotspots* a partial laminectomy was performed over T11-T13 spinal segments, or over the L2 spinal segment. Stimulating electrodes were created by removing a small part of the insulation (~400 μm notch) from Teflon-coated stainless-steel wires (AS632, Cooner Wire, USA), which were subsequently secured at the midline by suturing the wires to the dura. A common ground wire (~1 cm of Teflon removed at the distal end) was inserted subcutaneously. Stimulation in these cases was driven by an external stimulator (A-M Systems). To insert and stabilize e-dura implants into the epidural space two partial laminectomies were performed at vertebrae levels L1–L2 and T8–T9 to create entry and exit points for the implant. The implant was gently pulled above the dura mater using a surgical suture[34]. Electrophysiological testing was performed intra-operatively to fine-tune positioning of electrodes. The connector of the implant was secured into a protective cage plastered using freshly mixed dental cement on top of the L2–L3 vertebra. Stimulation was then delivered through an IZ2 stimulator (Tucker- Davis Technologies; see **Closed loop hemodynamic monitoring platform and control policies**[21]).

Dorsal rhizotomy
Under urethane anesthesia a laminectomy was performed to expose the T11-T13 posterior roots. The laminectomy was laterally expanded to expose the dorsal root ganglia. The posterior roots were systematically cut bilaterally using microscissors. This procedure was completed in the presence of either T12 or L2 EES (see **Extended Data Figures 3 & 4**).

Splanchnic ganglia manipulations
For experiments involving manipulation of the splanchnic ganglia, a midline laparotomy was performed. The hepatic portal vein, inferior vena cava, and abdominal aorta were gently retracted. The surrounding fascia was bluntly dissected to expose the celiac, superior mesenteric, and inferior mesenteric ganglia. At this point either stimulation was applied (see *Rodent electrophysiology*) or an axotomy was performed to sever the connection from the spinal cord to the ganglia.

Hemodynamic and sympathetic nerve activity monitoring

We recorded blood pressure and sympathetic nerve activity chronically (see **Extended Data Figure 1 and 2**) using wireless telemeters (TRM56SP SNA and Pressure Telemeter, Kaha sciences). A midline abdominal incision was made to expose the peritoneal cavity, followed by a blunt dissection to reach the descending aorta. The aorta was temporary occluded using a 4-0 silk, one to two millimeters rostral to the iliac bifurcation. The pressure sensor was inserted in the aorta so that the tip was just caudal to the renal artery, and fixed with a surgical mesh and biocompatible surgical glue. Following the catheterization of the aorta, the renal nerve was exposed immediately caudal to the right kidney. A micro electrode wire was sutured to the renal nerve using 8-0 silk sutures (Ethicon, USA), and the ground was left freely in the peritoneal cavity. The quality of SNA recordings was assessed weekly. Since conventional approaches, such as exposure to stress-evoking high-frequency noise, could not be used in rats with complete SCI, we devised a new paradigm based on the recruitment of afferents below the level of injury. We pinched the tail to evoke a noxious stimulus that triggered activity in the nerve recording. For each rat, we ensured that the signal remained stable and responsive. Analgesia (buprenorphine, Essex Chemie AG, Switzerland, 0.01–0.05 mg per kg, s.c.) and antibiotics (Amoxicillin 200mg/4ml Sandoz, Germany, 200mg/L *ad libitum*) were provided for 3 and 5 days after surgery, respectively. In some cases, a carotid catheterization was used for terminal experiments. Briefly, following anesthesia induction, the hair on the neck was shaved, and the surgical site cleaned with alcohol and betadine. The right common carotid artery was exposed and isolated from the internal jugular vein using blunt dissection. The carotid artery was then permanently occluded rostrally and temporarily occluded caudal to the implantation site using 4-0 silk sutures. A small incision was made in the artery wall using a bent tip 20 gauge needle and the blood pressure device guided into the lumen and advanced caudally to approximately 5-6mm rostral to the aortic arch. The catheter was then secured with two 4-0 silk sutures [47].

For non-human primates a large-animal catheter (AD Instruments, MPR-500; 5F) was inserted into the subclavian artery according to the same surgical procedures described above. In all cases, for rodents and non-human primates, data was collected, analog-to-digital converted (PowerLab; AD Instruments, CO, USA), and sampled at 1000Hz (LabChart; AD Instruments, CO, USA).

Intravenous lines

Rodent intravenous drug delivery was performed via a femoral venous line. For non-human primate experiments, propofol and required fluid management was delivered intravenously via a dorsal venous arch line.

Implementation of a simulated orthostatic challenge in rodents and non-human primates

A custom-made servo-controlled lower body negative pressure (LBNP) chamber was manufactured to induce a controlled reduction of arterial pressure in rodents (see **Extended Data Figure 1**). Animals were placed inside a sealed rectangular prism (dimensions: 25.5cm long, 14cm wide, 13cm height) from the feet up to the xiphoid process in the prone position. Negative pressure was induced using a vacuum pump attached to an electro-pneumatic regulator (SMC series ITV2000-Q) that allowed precise control of the pressure inside the chamber. Analog output of the chamber pressure from the regulator was fed through a DAQ USB device (NI USB-6001) to a computer running LabView. Using the same DAQ connection custom software was developed to induce preset pressure changes, while the pressure in the chamber is monitored in closed-loop

to ensure a constant orthostatic stimulus. Using this approach, we found that a stimulus of -10 mmHg led to a reproducible drop in hemodynamics that uninjured animals could recover from, but were unable to respond to after SCI (**Extended Data Figure 2h-j**).

For non-human primates we custom-built a larger lower body negative pressure system (**Extended Data Figure 9 Step 6**). To create a negative pressure environment inside the LBNP chamber a 3-stage 120V AC (368W) vacuum motor (Model 116565-13, AMETEK-Lamb Electric, Kent, OH, USA) with a 145mm diameter compressor housing (38mm diameter inlet) and 48mm diameter exhaust was used. The vacuum motor was regulated by an AC variable motor speed control (Model KBWC-115K, KB Electronics, Coral Springs, FL, USA) to vary the frequency cycle of the vacuum motor and manipulate the vacuum pressure produced. Vacuum pressure was measured via 5mm polyurethane tubing that ran from the LBNP chamber interior to a dual-port on-chip 4 pin pressure sensor (Model MPX2050DP, NXP Semiconductors, Eindhover, Netherlands) which produced an analog signal (mV) integrated by a PCB-ADC board. The converted values in mmHg were displayed via an LCD display (Model DMS-20LCD-0-5B-C, Murata Power Solutions, Kyoto, Japan). The analog reading from the pressure sensor was also wired from the PCB carrying the analog pressure signal to be recorded and visualized in parallel with physiological metrics via the Powerlab (PowerLab, AD Instruments, CO, USA) and LabChart software (LabChart, AD Instruments, CO, USA). A linear power supply (Model IHBB512, International Power, Oxnard, CA, USA) was used to convert the 120V AC input to a 12V DC output (1.2A) to provide the appropriate voltage to the pressure sensor, LCD display, and a brushless air exchange fan. The components were mounted and secured in an aluminum chassis, which was framed with acrylic plexiglass panels to form the vacuum unit. A 120mm DC brushless fan (Model OD1238-12HSS, Orion Fans, Dallas, TX, USA) was used to exhaust warm air from the interior of the vacuum unit during operation. The vacuum unit was attached to the LBNP chamber via 2.75m (30mm diameter) of flexible PVC Schedule 40 tubing. The ends of the tubing were fitted with reducing couplers (42mm OD to 30mm ID). The vacuum end was secured to a custom housing on the base of the vacuum unit which connected the vacuum intake port with a 43mm (ID) PVC coupler. The chamber end was connected via a 43mm (ID) female end, which was coupled to a 30mm (OD) x 20mm NPT male stud threaded into the base of the LBNP chamber and secured with adhesive to prevent any leaks. The exterior body of the LBNP chamber was made from polyethylene, structurally supported by an interior frame made from 32mm diameter PVC piping. A custom nylon cover was fitted around the chamber, and extended approximately 0.5m from the top of the chamber. Upon non-human primate placement in the chamber, the animal was secured and an airtight seal created. To ensure consistent non-human primate positioning during negative pressure, a custom seat with an adjustable range of approximately 240mm was manufactured from 32mm (diameter) PVC piping, and was secured to the interior frame via a PVC tee joint.

Visualization of the anatomical features of the thoracic spinal cord

Microcomputed tomography in rodents

Repeated imaging of the thoracic spinal column was conducted using the microcomputed tomography scanner Skyscan 1076 (Bruker µCT), as we have previously described[21]. The resulting projection images were reconstructed into 3D renderings using NRecon and GPURecon Server (Bruker µCT). Segmentation and 3D models were constructed with Amira (FEI Vizualisation Sciences Group). The shape of vertebrae was measured using microcomputed tomography imaging. The spinal cords of one rat was imaged, and the entire bone structure was reconstructed

in 3D. The 3D renderings were exported in the virtual reality modeling language file format WRL that was later merged with spinal tissue and dorsal root reconstructions.

Magnetic resonance imaging in rodents
The rodent's spinal cord was imaged post-mortem in a 9.4T MRI system (Magnex Scientific, Abingdon, UK), equipped with 400 mT/m gradients and interfaced to a DirectDrive console (Varian, Palo Alto, CA) using a custom-made volume quadrature radio frequency coil. High-resolution images of the spinal cord were acquired using a multi-slice fast-spin-echo sequence (TE/TR = 12.5/5000 ms, echo train length = 4) yielding 0.1 x 0.1 mm^2 in-plane resolution and 120 1-mm slices covering the entire cord.

Measurements of spinal segment morphologies on fresh tissue
For each subject (n = 3 rodents; n = 3 non-human primates), the spinal segments were identified on the basis of the innervation of the dorsal roots. The center of the segment was defined as the entry point of the rootlets. After measuring the length of vertebra and the relationships between vertebra and spinal segments, the entire spinal cord was extracted and the roots moved perpendicular to the spinal cord to clearly visualize the segments. The location and length of each segment was then calculated.

Design, fabrication and characterisation of soft electrode arrays – e-dura
The implant manufacturing follows the silicone-on-silicon process, enabling wafer-scale fabrication and the design freedom required to produce devices adapted for both rat and non-human primate models. Briefly, electrode arrays were fabricated in a class 100 cleanroom environment by embedding thin-film gold tracks between two layers of silicone rubber (Polydimethylsiloxane, PDMS, Sylgard 184, Dow Corning) to form stretchable interconnects[34]. The top silicone layer includes vias that define active stimulation sites, through which a soft composite coating is screen printed onto the gold. The coating material is fabricated by dispersing meso-scale platinum particles (Strem Chemicals inc., 0.27-0.47 µm average size) within a PDMS matrix, in order to create a conductive paste that offers a balance between the charge transfer properties of platinum, a roughened surface for increased equivalent area and the mechanical properties of PDMS.

Two different 6-polar implant layouts were used for rats and non-human primate models, with dimensions adapted to the different anatomical scales. Electrodes were designed with a circular shape (500 µm diameter) for rats and rectangular (0.7 mm by 2 mm) for non-human primates. The resulting geometric surface areas (GSA) for the two designs are about 0.002 cm^2 and 0.014 cm^2, respectively. The total device thickness was about 100 µm for rat implants and 400 µm for non-human primate implants, in accordance with the dimensions of the vertebral columns for each species. Devices were sterilized using ETO.

Rat implants were connected via stainless steel wires (Cooner Wire) to 12-contact Omnetics Micro 360® connectors (6 used as stimulation channels connected to the separate electrodes on the array, and 6 as stimulation ground in vivo). Non-human primate implants were connected to standard 8-polar implantable leads.

Prior to implantation, the arrays were characterised in vitro by acquiring electrochemical impedance spectra (EIS) of the electrodes in Phosphate Buffered Saline solution (Gibco PBS, pH 7.4, 1X), using a platinum wire as a counter electrode and an Ag|AgCl reference electrode (Metrohm, El. Ag/AgCl DJ RN SC: KCl). In this 3-electrode configuration, EIS measurements were

taken at room temperature using a Gamry Instruments Reference 600 potentiostat (100 mV amplitude, 1 Hz – 1 MHz frequency).

Virus production

Viruses used in this study were acquired commercially. The following virus was obtained for tract tracing: AAV-DJ-hSyn Flex mGFP 2 A synaptophysin mRuby (Stanford Vector Core Facility, reference AAV DJ GVVC-AAV-100, titer 1.15E12 GC/ml[26]). Optogenetics experiments were carried out using AAV5-EF1a-dio-eNpHR3.0-RFP-WRPE[31] (v203-5 from Viral Vector Faciltiy VVF, Neurosciences Center Zurich (ZNZ); titer 5.6E12 VG/ml), AAV5-CAG-eNpHR3.0-eYFP[31] (Gene Therapy Center Virus Vector Core Facility, The University of North Carolina; titer 6E12 VG/ml), and AAV5-Ef1a-DIO-hChR2 (H134R)-eYFP (Gene Therapy Center Virus Vector Core Facility, The University of North Carolina; titer 4E12 VG/ml). AAV5 production was carried out in 293AAV HEK cells following standard procedures, yielding vector suspensions with the following titers: AAV5-CMV-cre (1.12E12 VG/ml). All flexed AAV vectors used in the present study showed transgene expression only upon Cre-mediated recombination. Injection volumes, coordinates and experimental purpose using these viruses are described specifically below. Pseudorabies tracing was completed using Bartha strain PRV152 (expressing GFP; 4.9 × 109 pfu per ml, Princeton University).

Viral injections

Brainstem injections were performed through stereotaxic injections using high-precision instruments under isoflurane anesthesia. All anterograde tract-tracing and optogenetic experiments manipulating rostral ventrolateral medulla (RVLM) neurons were performed in TH-Cre rats[27]. A craniotomy was performed bilaterally over the brainstem medulla oblongata and AAV-DJ hSyn FLEX-mGFP 2A Synaptophysin-mRuby (titer 1.15E12 GC/ml[26]) was injected into the RVLM. Four injections (250nl per injection) at two different rostrocaudal locations at two depths were made bilaterally. Coordinates used for targeting this nucleus were -12.12 to -12.62 mm anteroposterior from Bregma, 2 mm lateral and 7.8 to 8 mm ventral from the surface of the cerebellum[51]. Injections were performed using the Hamilton injection system. Viruses were injected and the needle was held in place for 2 minutes before being slowly retracted[48]. For splanchnic ganglia injections, a midline laparotomy was performed. The hepatic portal vein, inferior vena cava, and abdominal aorta were gently retracted. The surrounding fascia was bluntly dissected to expose the celiac, superior mesenteric, and inferior mesenteric ganglia. Viruses were injected at 0.2 µl per minute using glass micropipettes connected via high pressure tubing (Kopf) to 10-µl syringes under the control of microinfusion pumps. After injection of the tracer, the abdominal muscle wall and skin were closed with 5-0 monocryl and 5-0 prolene sutures, respectively. Dorsal root ganglia injections were completed by exposing the T12 dorsal root ganglia with a laminectomy. Viruses were injected under stereotaxic guidance at 0.2 µl per minute using glass micropipettes connected via high pressure tubing (Kopf) to 10-µl syringes under the control of microinfusion pumps.

Fluorogold tracing

0.4% Fluorogold in distilled water (fluorochrome) was injected into either the splanchnic ganglia (2 µl) or the intraperitoneal cavity (100 µl) 7 days before perfusion[52].

Rodent electrophysiology

For stimulation of the rostral ventrolateral medulla and splanchnic ganglia, a tungsten bipolar concentric electrode was positioned either in the rostral ventrolateral medulla (Coordinates: -12.12 to -12.62 mm anteroposterior from Bregma, 2 mm lateral and 7.8 to 8 mm ventral from the surface of the cerebellum) or immediately on top of the splanchnic ganglia. Three silver ball electrodes were used to record any evoked activity from the surface of the exposed spinal cord at various locations (over the T11, T12, and T13 roots), as we have previously described for other contexts[46]. Stimulation was delivered in 200 µs square wave pulses at the maximum amplitude possible before large motor responses were evoked (typically between 600 µA and 800 µA) and at a frequency of 1 Hz using a STG 4004 stimulus generator (Multi Channel Systems). Evoked activity was amplified and recorded using an A-M systems differential amplifier, PowerLab and LabChart Pro acquisition and analysis system (AD Instruments). For analysis, 100 action potential traces from each recording site were averaged and the peak to peak delay of the evoked potential was quantified.

Optogenetics experiments

Animals were anesthetized with urethane (see **Rodent Anesthesia Use**) in order to preserve spinal reflexes during the experiment. A carotid catheterization was first performed to record blood pressure and a monopolar electrode was fixed to the T12 segment for epidural stimulation. A laser was secured to a stereotax, and positioned directly over top of either the splanchnic ganglia (see **Extended Data Figure 5**). Systolic, diastolic, and mean arterial pressure were then derived on a beat-by-beat basis over 10 minutes to establish resting hemodynamics. Once resting hemodynamics were established, EES was then delivered at 50Hz, with a pulse length of 2ms, and the current increased from 0 to approximately 200mA. Upon visible motor threshold, the stimulation was stopped. Once the appropriate amplitude for stimulation was established, trials were performed by taking 30 seconds of hemodynamic baseline, followed by 10 seconds of stimulation alone and 30 seconds of laser combined with stimulation. A laser (Laserglow, 589 nm Yellow DPSS Laser System) transmitted yellow light through an optic fiber (200 µm core diameter, 0.22 NA, Thorlabs) that was held in a 1.25-mm ferrule at the surface of the ganglia. Light stimulation was delivered over 10 s and consisted of 10-ms-long pulses delivered at 40 Hz[48]. Following completion of the experiment, the animal was overdosed with urethane. The celiac ganglia were dissected and postfixed.

   For optogenetic manipulation of the rostral ventrolateral medulla, optic fibers were implanted immediately following virus injection (see **Viral injections**) in the right and left RVLM using the coordinates previously described (–12.6 mm anteroposterior, 2 mm lateral, –7.8 mm ventral). The ferrule was fixed with dental cement. Light was transmitted to the brain through a ferrule-to-ferrule connection cable[48]. Laser pulses were driven by an external stimulator (A-M Systems) to ensure precise control of stimulation features. Light stimulation was delivered over 10s and consisted of 10ms-long pulses delivered at 40 Hz[48]. Experiments were completed under urethane anesthesia with blood pressure monitoring in place.

Pharmacological experiments

For pharmacological experiments drugs were infused as a bolus through an intravenous line. Doses were determined based on pilot experiments and *in-vivo* experimental confirmation. Drug doses included sodium nitroprusside: 10 µg/kg, and prazosin: 10 µg/kg.

Hybrid computational model of the rat spinal cord

We previously developed and validated experimentally a hybrid computational model of EES of the lumbar and sacral regions of the rat spinal cord[11,30]. We extended this effort to create a hybrid computational model of the lower thoracic and upper lumbar segments of the rat spinal cord. For this purpose we acquired high-resolution MRI-datasets of the rat spinal cord and manually segmented the white matter (WM), spinal roots, cerebrospinal fluid (CSF) and vertebral bone to create a realistic 3D reconstruction of the thoracic and lumbar spinal cord of a rat. We artificially filled the epidural space between the bone and CSF and assigned it as the material epidural fat. Additionally, we utilized tracings of the grey matter (GM) of rats and scaled them to the size of the WM to create this material. We then placed this model in a large saline conductor to represent the remaining body of the rat. We assigned the same conductivity values as previously to this model[30] and calculated the electric fields elicited by electrical spinal cord stimulation utilizing a finite element approach. The models were all implemented in Sim4Life v3.4 (ZMT Zürich MedTech AG) [36].

Furthermore, we combined these solutions with anatomically and biophysically realistic neural structures to derive the type of fibers and neurons activated by the stimulation[53,54]. We then coupled these activation maps with a purely hypothetical network model composed of integrate-and-fire neurons that connected to an approximation of pre-ganglionic neurons. Three network architectures were tested. The connection was mediated through either monosynaptic, disynaptic excitatory, or disynaptic inhibitory pathways. Electrophysiological parameters were recorded in-silico at all neuron populations.

Hybrid computational model of the human spinal cord
We repeated the same procedure as in **Hybrid computational model of the rat spinal cord** with MRI and CT datasets of a human patient implanted with the MDT 5-6-5 array. We identified optimal multipolar stimulation parameters by utilizing a genetic algorithm to target the lower thoracic spinal roots[30].

Closed loop hemodynamic monitoring and stimulation platform and control policies
Our closed loop monitoring and control platform was implemented within a multi-threaded C++ code (Visual Studio 2010, Microsoft) running on a quad-core Microsoft Windows 7 computer. Stimulation patterns were applied via an RZ5 processing unit (Tucker- Davis Technologies) connected to an MS16 Stimulus Isolator (Tucker-Davis Technologies)[21]. The integrated hemodynamic recording system generated a raw blood pressure trace, which was imported into the C++ environment in (soft) real-time through the accompanying DAC on the RZ5 processing unit. The control logic delivered stimulation to electrodes based on the trajectory of mean blood pressure or the sum firing rate derived from the RVLM. Control algorithms continuously calculated the deviation of blood pressure from the mean. The change in amplitude for electrode configuration was continuously adjusted and scaled according to a proportional and an integral coefficient. This continuous control was further modulated by key biomimetic features. Specifically, our electrode array consists of paired electrodes at three key hemodynamic hotspots. Therefore, we integrated a biologically-relevant delay (2.5ms) between each segment, in line with conduction delays that were experimentally tested (**Extended Data Figure 6**). Furthermore, to re-integrate the frequency dynamics lost after SCI (**Extended Data Figure 6** and **Figure 3**), we continuously adjusted the amplitude of stimulation between 90% and 100% at the relative frequency of Meyer waves in each species (e.g., rat: 0.4 Hz, non-human primate: 0.1 Hz; human: 0.1 Hz). Stimulation was then delivered using an IZ2 stimulator (Tucker- Davis Technologies) to

stimulation arrays. This custom control software therefore delivered all the key components of the biomimetic stimulation. Custom-developed C++ and Tucker-Davis Technologies codes can be made available through material transfer agreement upon reasonable request.

For non-human primate experiments EES was delivered using clinical grade technologies (n = 3). Stimulation was delivered with an IPG (Medtronic Activa™ RC) that enabled monopolar and multipolar stimulation at constant current or constant voltage through one or a subset of the 6 electrodes of the custom designed non-human primate array or the case of the IPG (anode). The IPG was modified from its clinical version with an investigational firmware that enabled real-time communication with a software running on an external computer (NEUWalk Research Programmer Application NRPA, Model 09103, Medtronic[11]). The NRPA acted as a relay between EES triggering commands sent by the control software (conceptually described above), which we implemented in a compatible Python package and accompanying C# interface. It communicated wirelessly with the IPG through the following communication chain: the NRPA sent commands via a virtual COM port corresponding to a Bluetooth adapter, which received this command and forwarded it to a virtual COM port 6 corresponding to a USB adapter, a USB to infrared adapter (ACT-IR224UN-LN115-LE, ACTiSYS Corporation, Fremont, CA, USA) transformed this command into infrared signals that were then read by a modified Medtronic patient's programmer (Sensing Programmer Telemetry Module SPTM, Medtronic), which finally transmitted the command to the patient's IPG by electromagnetic induction through the skin (see **Extended Data Figure 8**). Thus, our custom control software interacted with this clinical grade stimulation in closed loop, while also delivering all the key components of the biomimetic stimulation, including delays between each of the 3 segments as well as a 0.1 Hz overlay to ensure the dynamics of the system were recapitulated.

Rodent perfusion protocol

For all rodent perfusions, animals were anesthetized by an i.p. injection of 0.5ml Pentobarbital-Na (50 mg/mL; PBS) and transcardially perfused with approximately 80ml Ringer's solution containing 100'000IU/L heparin (Liquemin, Roche, Switzerland) and 0.25% NaNO2 followed by 300ml of cold 4% phosphate buffered paraformaldehyde, pH 7.4. The tissue was removed and postfixed in the same fixative before they were transferred to 30% sucrose in phosphate buffer (PB) for cryoprotection, or placed in PBC prior to tissue clearing [48]. Prior to cryosectioning tissue was embedded in Tissue Tek O.C.T (Sakura Finetek Europe B.V., The Netherlands) and frozen at -80°C.

Tissue clearing and imaging of rat brainstem and spinal cord

Rat brainstem and spinal cord were cleared using uDISCO [55] and CLARITY[56], respectively, four weeks after injection of AAV-DJ-hSyn-flex-mGFP-2A-Synaptophysin-mRuby[26]. Rats were perfused transcardially first with 0.1 M PBS followed by 4% PFA (in 0.1 M PBS, pH 7.4) at 4°C. The rat brainstem (to visualize the rostral ventrolateral medulla injection site) and thoracic spinal cord (to visualize the contusion lesion) were dissected and post-fixed in 4% PFA (in 0.1 M PBS) for 24 hours at 4°C. The dura was removed from the samples prior to clearing.

uDISCO clearing of rat brainstem

uDISCO clearing of the rat brainstem was initiated with step-wise dehydration in increasing concentrations of tert-butanol dissolved in dH2O with a total volume of 5 mL at 35°C as follows: 30% tert-butanol overnight, 50% for 10 hours, 70% overnight, 80% for 10 hours, 90% overnight, 96% for 10 hours, and 100% overnight. The sample was then incubated in 5 mL of dichloromethane at room temperature for 70 minutes with shaking. This was then followed by

incubation in BABB-D4 (BABB: 2:1 mixture of benzyl benzoate to benzyl alcohol; 4:1 mixture of BABB to diphenyl ether; 0.4% v/v vitamin E) for 24 hours at room temperature prior to imaging.

CLARITY clearing of rat spinal cord
To initiate CLARITY of the rat spinal cord, the sample was incubated in A4P0 hydrogel solution (4% acrylamide in 0.001M PBS with 0.25% of the photoinitiator 2,2'-azobis[2-(2-imidazolin-2-yl)propane] dihydrochloride (Wako Pure Chemical, Osaka, Japan)) for 24 hours at 4°C with gentle nutation. The sample was then degassed by bubbling nitrogen gas through the tube for 3 minutes then quickly and tightly closing the tube cap. Hydrogel polymerization was then initiated by incubating the sample in a 37°C water bath for 2 hours. Excess hydrogel was removed, and tissue was washed in 0.001 M PBS for 5 minutes at room temperature. The sample was then placed in the X-CLARITY Tissue Clearing System I (Logos Biosystems Inc., South Korea) set to 1.2 A, 100 RPM, 37°C. Clearing solution was made in-house and consisted of 40 g of sodium dodecyl sulfate (SDS), 200 mM boric acid, and filled to a total volume of 1 L with dH2O (pH adjusted to 8.5). The sample was cleared after about 10-15 hours. After clearing, the sample was washed for at least 24 hours at room temperature with shaking in 1x PBS and 0.1% Triton-X (with 0.02% sodium azide) to remove excess SDS. The sample was then incubated in RIMS (40 g of Histodenz dissolved in 30 mL of 0.02 M PB, pH 7.5, 0.01% sodium azide, refractive index 1.465) for at least 24 hours at room temperature with gentle shaking prior to imaging.

Imaging was performed using a custom-built CLARITY-optimized light-sheet microscope (COLM) as described previously[28]. A customized sample holder was used to secure the brainstem or spinal cord sample in a chamber filled with BABB-D4 (uDISCO) or RIMS (CLARITY). Samples were imaged using a 10x (injection site) or 4x (lesion) objective with two lightsheets illuminating the sample from the left and the right sides. The pixel resolution for the 10x acquisition was 0.48 x 0.48 x 3 μm and 1.4 μm by 1.4 μm by 5 μm for the 4x acquisition in the x-, y-, and z-directions. Images were acquired as 16-bit TIFF files and reconstructed in 3D using TeraStitcher[57]. 3D reconstructions of the raw images were produced using Imaris (Bitplane, v.9.0.0). The spinal cord lesion reconstructions were performed manually using Imaris.

Immunohistochemistry
Immunohistochemistry was performed according to the following procedures[48]. First, sections were thawed for one hour at room temperature. Next, sections were rehydrated in PBS for 10 minutes. Normal donkey serum (NGS, Millipore) was then placed on the slides for 30 minutes. Lastly, primary antibodies (350 μl) were placed on the sections and allowed to incubate overnight. The following primary antibodies were used: guinea pig anti-neuronal nuclei (NeuN, 1:300, Millipore, ABN90P), rabbit anti-cFos (cFos, 1:500, Calbiochem, PC38), mouse anti-tyrosine hydroxylase (TH, 1:2000, Millipore, MAB318), mouse anti-glial fibrillary acidic protein (GFAP, 1:1000, Sigma-aldricht, G3893), mouse anti-vesicular glutamate transporter 1 (VGLUT1, 1:1000, Millipore, MAB5502), rabbit anti-choline acetyltransferase (ChAT, 1:50, Millipore, AB144P) and rabbit anti-alpha 1 Adrenergic Receptor (ADRA1, 1:500, Abcam, AB3462. Secondary antibodies included: Alexa Fluor 647 Donkey Anti Mouse (1:200; Life Technologies, A31571), Alexa Fluor 488 Donkey Anti Rabbit (1:200, Life Technologies, A21206), Alexa Fluor 488 Goat anti Rabbit (1:200, Life Technologies, A11008), Alexa Fluor 555 Goat anti Rabbit (1:200, Life Technologies, A21428), Alexa Fluor 555 Goat anti Guinea Pig (1:200, Life Technologies, A21435) and also DAPI (1:1000, Life technologies). Following the secondary staining, three additional washes with PBS

were performed and a Nissl stain was applied (1:100, Millipore). Immunofluorescence was imaged digitally using a slide scanner [Olympus VS-120 Slide scanner] or confocal microscope [Zeiss LSM880 + Airy fast module with ZEN 2 Black software (Zeiss, Oberkochen, Germany)]. Images were digitally processed using ImageJ (ImageJ NIH) software or Imaris (Bitplane, v.9.0.0).

Fluorescence in-situ hybridization
Interneurons trans-synaptically connected to splanchnic ganglia were examined for co-localization of Slc17a6 mRNA using the RNA labelling kit from Molecular instruments (Molecular instruments, USA). After perfusion, tissues were fixed in 4% phosphate buffered paraformaldehyde for 3 hours at 4°C before they were transferred to 30% sucrose in phosphate buffer (PB) for cryoprotection at 4°C for 2 nights. RNA in situ hybridization was performed on 40µm spinal cord sections. Samples were placed in 5x SSCT (20x SSC buffer, Invitrogen, USA; 10% Tween 20, Applichem, Germany) for 10min and then pre-hybridized in 30% probe hybridization buffer (Molecular instruments, USA) for 30min at 37°C. Samples were hybridized overnight at 2µM probe concentration in 30% probe hybridization buffer at 37°C. Following hybridization, samples were washed in a solution of 30% probe wash buffer (Molecular instruments, USA) and 5x SSCT four times 15 minutes. Sections were then incubated in an amplification buffer (Molecular instruments, USA) for 30min at room temperature. In the meantime, fluorophore-labeled HCR hairpins (Molecular instruments, USA) were snap-cooled (heating at 95°C for 90sec) and cooled down to room temperature. Amplification was performed overnight at room temperature at a concentration of 120nM per hairpin in the amplification buffer. Following amplification, samples were washed in 5x SSCT for at least 2 times 30min to remove unbound hairpins. Lastly, sections were air-dried and cover slipped using Mowiol (Calbiochem, USA).

Hemodynamic analyses
Classical orthostatic challenge using a tilt test
Baseline values for hemodynamics (i.e., systolic blood pressure, mean arterial pressure, diastolic blood pressure) were recorded over five minutes. Next, animals (n=4) were tilted 90 degrees upright while secured to a platform for three minutes in order to maximally challenge animals against gravitational forces. Delta values were calculated compared to baseline for each animal, for each minute (see **Extended Data Figure 1**).

Response to spinal cord injury
Resting systolic, diastolic, and mean arterial blood pressure, as well as heart rate, were assessed over a ten-minute period prior to spinal cord contusion (see **Extended Data Figure 2**). Following this period, the experimenter initiated the Infinite-Horizons impactor (rodent) or forceps compression (non-human primate). The severity of the response to spinal cord contusion was assessed as the maximum change in blood pressure (systolic, diastolic, and mean taken independently) and sympathetic nerve activity (rodent only) over the following one-minute period. Next, the resulting neurogenic shock was quantified as the minimum blood pressure (systolic, diastolic, and mean taken independently) and sympathetic nerve activity (rodent only) following one hour.

Establishment of hemodynamic instability after spinal cord injury
Our comprehensive chronic analysis pipeline is predicated on generating an entirely automated analysis. Therefore, every aspect of the following methods requires no human intervention. First,

we calculated systolic, blood pressure, diastolic blood pressure, mean arterial pressure, and heart rate on each hour of data (save automatically). At this step we filtered out non physiological values (filter set with a HR < 180 beat per min (bpm) or > 625 bpm), then saved the detailed record of blood pressure for further analysis. Next, we removed outliers by binning each outcome in intervals of ten seconds, and computing the first principal component eigenvalue. We then performed hierarchical clustering (k = 2) to identify and remove remaining outliers. Next, we extracted the raw sympathetic nerve activity recordings. We first applied a second order Butterworth filter (100-500Hz) and rectified the signal. We then computed a ten millisecond windowed integral (i.e., 'iSNA'). Background levels of iSNA were measured in a post-mortem animal and subtracted from the final values. With our final dataset we then used a local polynomial regression to interpolate missing data points (e.g., during animal care). Data was then summarized hourly to generate a total of 1176 (24 hours and 7 weeks of data collection) datapoints per animal. We determined the frequency that each animal's values deviated outside clinically relevant thresholds using this final dataset. Thresholds were set at 100, 80, and 70 for systolic blood pressure, mean arterial pressure, and diastolic blood pressure, respectively. Finally, we calculated the variance for each outcome (e.g., systolic blood pressure), for each animal across the entire dataset.

Formal weekly hemodynamic assessments
First, resting beat-by-beat arterial pressure, heart rate, and sympathetic nerve activity were recorded for 10 minutes to calculate mean values. Next, animals were subjected to a negative pressure stimulus using our custom lower body negative pressure chamber. After five minutes of baseline the chamber pressure was reduced to -10 mmHg for one minute. We calculated the delta value for each outcome during the final 30 seconds of the chamber being on, compared to baseline, in order to best quantify the ability of each animal to recovery from the stimulus. Finally, we calculated a linear model between hemodynamic values and the exact chamber pressure.

Celiac ganglia stimulation recordings
Hemodynamic outcomes were recorded during stimulation of the celiac ganglia (see **Rodent electrophysiology**). Across step-wise increases in stimulation amplitude (range 0-400µV) delta values were calculated compared to baseline values. For visualization (see **Extended Data Figure 3**) delta values and stimulation amplitudes are scaled 0-100% for each animal (**n = 4**).

Spinal cord segment mapping of hemodynamic responses
Systolic, diastolic, and mean arterial pressure were derived on a beat-by-beat basis over 10 minutes to establish resting hemodynamics. The maximal hemodynamic response at each segment was extracted by taking 30 seconds of baseline prior to stimulation at that segment, and then the maximal blood pressure immediately prior to visible motor threshold. Therefore, one value (delta) was taken for: systolic blood pressure, diastolic blood pressure, mean arterial pressure, and heart rate for each segment, for each rat. Concordance between these values and sympathetic neuron densities (see **Anatomical segmental density distributions**) were then calculated using standard linear models. For non-human primates, n = 3 were used for functional mapping.

EES before and after successive dorsal rhizotomies

After establishing baseline hemodynamics EES was applied in order to induce a pressor response (**n = 5**). Delta values for each hemodynamic parameter (i.e., systolic blood pressure, diastolic blood pressure, and mean arterial pressure) were then derived. Next, successive bilateral dorsal rhizotomies (See *Dorsal rhizotomies* in **Surgical procedures and post-surgical care)** were completed beginning at T11 and finishing with T12. Between each rhizotomy EES was applied and delta values for each hemodynamic parameter calculated.

Optogenetic silencing
After establishing baseline hemodynamics EES was initiated and the peak hemodynamic value taken. After 10 seconds of EES a laser was initiated for 30 seconds. The minimum value during this time period was then calculated. Finally, a blunting ratio was calculated as the ratio of the decrease between the peak EES values and minimum value during the silencing during experimental (laser ON) trials compared to control trials (see **Extended Data Figure 5**).

Splanchnic axotomies
After establishing baseline hemodynamics EES was initiated and the peak delta values calculated for each parameter. Next, a splanchnic axotomy was performed (See *Splanchnic ganglia manipulations* in **Surgical procedures and post-surgical care**). The same calculation procedures were then completed following axotomy (see **Extended Data Figure 5**).

Alpha1 receptor blockade
After establishing baseline hemodynamics, EES was initiated and the peak delta values calculated for each parameter. After prazosin infusion (10 µg/kg), EES was triggered every minute for 10 minutes and delta values calculated. The minimum response value was taken during this time. A washout value was calculated after 30 minutes, which we found was sufficient time for the response to be reinstated (see **Extended Data Figure 5**).

Establishing natural system dynamics
The relationships between systolic blood pressure, rostral ventrolateral medulla firing rate, and sympathetic nerve activity, recorded at the sympathetic renal nerve, were assessed using a feed-forward neural network. A basic regression model was implemented using the `keras` framework within R. We used a sequential model with two densely connected hidden layers, and an output layer that returns a single, continuous value. We then aimed to predict a given output (e.g., sympathetic nerve activity) from a given input (e.g., rostral ventrolateral medulla firing rate). We used an 20/80 test-train split, with each trial from each animal representing a discrete item. We evaluated the performance of the model for the uninjured and SCI groups separately using the significance of the correlation between the real and predicted output traces.

Wavelet decomposition
To assess the periodic content of a given time-series, wavelet decomposition was implemented using the `WaveletComp` R package. We analyzed the univariate frequency structure using the function `analyze.wavelet` function with default parameters.

Single versus multiple hemodynamic hotspot stimulation
After establishing baseline hemodynamics we assessed whether stimulating one hotspot (T12) was more or less efficacious than stimulating the three key identified *hemodynamic hotspots*. The

order of the stimulations was randomized, to avoid bias towards either single or joint stimulation. We assessed the maximum change in hemodynamics in response to the stimulation for each of the conditions. For non-human primates, n = 3 were used.

Closed-loop control of hemodynamics
The efficacy of closed loop protocols was established through key primary outcome measures. These included: 1) target error, defined as the difference between the 'target' (baseline) hemodynamic value and the actual value during an orthostatic stimulus; 2) time outside target, defined as the amount of time (s) spent outside a given target threshold (e.g., baseline blood pressure -10 mmHg), which were tuned according to the desired accuracy in a given situation; 3) the model coefficient of the linear relationship between the change in hemodynamics (e.g., systolic blood pressure) and the pressure inside the negative pressure chamber; 4) convergence, defined as the time until stabilization of hemodynamics (set conservatively at +/- 2mmHg); and 5) the time to max amplitude, in the case of the brainstem-spinal cord versus biomimetic control comparisons. For non-human primates, n = 2 were used.

Neuromorphological analyses
Anterograde axon and synapse quantification from the RVLM
Axon density (mGFP) was measured using 3 confocal image stacks per region (above: T1 spinal cord, below: L1 spinal cord) per animal (n = 4 rats). Images were acquired with standard imaging settings and analyzed using custom-written Fiji scripts according to previously described methods. Confocal output images were binarized by means of an intensity threshold and divided into square regions of interest (ROI). The investigator was blinded during intensity thresholding. Synapse density was quantified on each segmented sympathetic (ChAT[ON]) neurons using the area of each neuron and the area of colocalization, as defined using Squassh within ImageJ[58].

Evaluation of spinal cord contusion
The extent and location of spinal cord damage was evaluated in each experimental animal[48]. The lesion cavity was cut in serial horizontal sections (40 μm) that were stained using GFAP. For each lesion, we calculated the spared spinal cord surface with respect to the distance from the epicenter of the lesion, the spared area at the epicenter, and the total volume of damaged spinal cord tissue. The percentage of spared tissue at the epicenter was calculated using Fiji and normalized using the mean surface of sections rostral and caudal to the contusion, taking into account the compression of the spinal cord.

Anatomical segmental density distributions
To determine the segmental density of sympathetic pre-ganglionic neurons, neurons co-labeled with Fluorogold and NeuN were tabulated using ImageJ (Fiji, Version 1.0), in four key autonomic nuclei (intermediolateral nucleus, central autonomic nucleus, lateral funiculus, and the intercalated nucleus) every 200 mm within each segment from T6-L1 (see **Extended Data Figure 3**). Neurons from the left and right side were summed. Concordance between these counts and the response to electrical stimulation were examined by transforming the values into a 0-1 range for each segment and plotting them against the electrical stimulation.

Assessment of immediate early gene expression in splanchnic ganglia

To investigate the recruitment of the celiac ganglia by our stimulation protocol, immunohistological staining for cells activity markers were performed on two groups of Lewis rats (see **Extended Data Figure 5**). For the first group (n = 5) animals were anesthetized with urethane and stimulated for 30 minutes at T12. Our second group (n = 5) was a control, animals were anesthetized with urethane for an hour, then overdosed with urethane. Stained sections were analyzed using confocal microscopy (Zeiss LSM 800 with airyscan) resulting in high resolution multi channels images, with 15 to 20 identifiable cells on each. We then built a custom analysis pipeline able to automatically segment, localize, and quantify cell colocalization across the three key phenotypic parameters (Nissl+TH, Nissl+cFos, TH+cFOS). Briefly, we implemented preprocessing steps using Fiji, as we have described[48]. Next, we leveraged a recently published pipeline for automated segmentation and colocalization[58]. For each channel, the optimal set of parameters were identified and used for all downstream analyses. All data were summarised and final quantifications completed using custom R scripts.

Dynamic registration and permutation test to determine spatial enrichment of histological signals
To determine spatial enrichment of axon density in the lateral horn of the spinal cord we implemented a custom image analysis pipeline that includes preprocessing, registration and combination of histological images from different rats. Briefly, we implemented all preprocessing in Fiji, and all registration procedures in R, using the image analysis package `imageR`, and medical image registration package `RNiftyReg`. Following dynamic registration, we determined the spatial enrichment of histological signals using custom R scripts, based on a permutation procedure. We first define a region of interest and compute the intensity of fluorescence for this area. We then randomly generate one thousand permutations of our region of interest over the image, allowing us to compute the null distribution of the signal and test the region of interest against it. Empirical p values were then calculated.

Statistical procedures
All data are reported as mean values and individual data points. No statistical methods were used to predetermine sample sizes, but our sample sizes are similar to those reported in previous publications[48]. Hemodynamic assays were replicated three to five times, depending on the experiment, and averaged per animal. Statistics were then performed over the mean of animals. All statistical analysis was performed in R using the base package `stats`, with primary implementation through the `tidyverse` and `broom` packages. Tests used included one or two-tailed paired or independent samples Student's t-tests, one-way ANOVA for neuromorphological evaluations with more than two groups, and one- or two-way repeated-measures ANOVA for hemodynamic assessments, when data were distributed normally, tested using a Shapiro-Wilk test. Post hoc Tukey tests were applied when appropriate. For regressions, mixed model linear regression was used in cases of multiple observations, or else standard linear modelling. In cases where group size was equal to or less than three null hypothesis testing was not completed. The significance level was set as P < 0.05. Exclusions of data is noted in the relevant methods sections.

Clinical implementation in humans
Patient description
The patient was a 38-year-old male who experienced a traumatic SCI at the C5 spinal segment treated with cervical fixation one year before enrollment in the study. The neurological status was evaluated according to the American Spinal Injury Association Impairment Scale (AIS) [59], and was

classified as motor and sensory complete (AIS-A; **Extended Data Fig. 10a**). Before enrollment, the patient was using 2.5 mg of midodrine hydrochloride 1-2 times per day as well as abdominal binders and compression garments daily to manage orthostatic hypotension.

Electrode array placement of electrical epidural stimulation implant
The patient underwent an array implantation of a three column (5-6-5), 16-contact paddle lead positioned below the T10 and T11 vertebral bodies and connected to a primary cell implantable pulse generator (IPG) (RestoreAdvanced™ SureScan™ neurostimulator, Medtronic, Minneapolis, MI) (See **Extended Data Figure 10**). The array was implanted over the T10-L1 spinal segments, which provides coverage over the hemodynamic hotspots identified in rats and non-human primates. The final positioning of the array was confirmed with computed tomography (CT; Revolution GSI, GE Healthcare, USA) as well as T1 and T2- weighted imaging acquired using a1.5-T MRI Optima MR450w Scanner (Optima™, GE Healthcare, USA). These acquisitions allowed for the visualization of the spine, spinal cord, and site of injury (*see* **Extended Data Figure 10**), and verification of the final medio-lateral and rostro-caudal positions of electrode array, relative to spinal column. Clinical testing was approved by the University of Calgary Research Ethics Board (REB18-1592, REB19-0349).

Orthostatic challenge using a clinical tilt test
All test procedures were performed at least one month after surgical implantation of the electrode array. Prior to test days, the patient was informed to abstain from vigorous exercise for 24 hours before testing, as well as to have abstained from caffeine, alcohol, cannabis, and withhold medications 12 hours prior to testing. The patient was also informed to only consume a light breakfast the day of testing. Upon arrival during testing days, the patient was transferred to a table capable of head-up tilt (Model 1211, MPI, Kansas City, USA) with feet positioned on a footrest in an abducted position (see **Extended Data Figure 10**). We applied restraint straps to secure the patient below the knees and across the thighs, with the feet stabilized. The upper body was secured by two restraint straps that went from the hip region across to the contralateral shoulder. Resting supine blood pressure were recorded continuously for approximately 5 minutes to establish baseline values. We then tilted the patient upright up to a maximum of 70 degrees while recording hemodynamic values and symptoms of orthostatic tolerance. Time to reach desired tilt angle from supine was achieved in less than 5 seconds.

Hemodynamic monitoring
Beat-to-beat blood pressure and heart rate was obtained via finger plethysmography (Finometer, Finapres Medical Systems; Amsterdam, Netherlands) and collected using an analog to digital converter (PowerLab, AD Instruments, CO, USA) at a sampling rate of 1,000 Hz (LabChart, AD Instruments, CO, USA). Beat-by-beat blood pressure was calibrated to brachial artery blood pressure collected using an arm cuff embedded and synchronized with the Finometer[60-64]. Heart rate, systolic, and diastolic pressures were recorded continuously throughout testing.

Symptoms of orthostatic intolerance
The patient was asked approximately every 1-3 minutes about their symptoms of orthostatic intolerance. The patient was asked to rank their symptoms between 1-10, 1 being no symptoms at all, and 10 being feelings of dizziness, lightheadedness[17], or nausea[17,25]. The patient was instructed to notify the research team if they needed to be returned to the supine position.

Blood draws and circulating norepinephrine
Two 6 mL blood samples were obtained from the median cubital vein using a sterile 21 gauge straight needle during stimulator-off and stimulator-on conditions. To avoid false positives, the patient was asked to abstain from any beta-blocker, dihydropyridine calcium channel blocker, phenoxybenzamine, anxiolytics, or decongestants medications. Blood draws occurred after approximately 30 minutes resting in the supine position. Samples were collected in mauve top CATP tube (Special Catecholamine collection tube K2 EDTA with sodium metabisulfite). To ensure sample quality, prior to and immediately after, collection tubes were kept cold via immersion in crushed ice and kept in foil to reduce exposure to light. Samples were centrifuged for 10 minutes at 4°C ± 2°C and a speed of 1200 relative centrifugal force (RCF). A minimum of 2mL extracted plasma from each tube (n=2 per condition) was analyzed for catecholamines (norepinephrine, epinephrine, dopamine) by Calgary Lab Services (Calgary, Alberta, Canada) using high performance liquid chromatography electro-chemical detection (HPLC-ECD).

Sympathetic nerve activity recordings
Microneurography was used to acquire efferent postganglionic muscle sympathetic nerve activity (MSNA) from the right common peroneal (fibular) nerve[65,66]. Palpation was used to locate the position of the common fibular nerve, followed by percutaneous insertion of a 2-MΩ tungsten microelectrode (FHC, Bowdoin, ME) into the nerve ~2 cm adjacent to a subcutaneous low impedance reference electrode. The MSNA signal was amplified (75,000x) and band-pass filtered (0.7– 2.0 kHz) to obtain the raw neurogram (i.e. muscle sympathetic spike activity) and then rectified and integrated (0.1-s time constant) to obtain a multi-unit (mean voltage) neurogram (Nerve Traffic Analyzer, Model 662C-4; University of Iowa, Iowa City, IA). Due to the impaired supraspinal influence on lower limb MSNA in this patient, there was a lack of spontaneous multi-unit MSNA bursts at rest and visually undetectable changes in neural activity during end expiratory apneas.[67] Thus, the recording microelectrode was confirmed to be near nerve fibres directed towards skeletal muscle by auditory feedback during tapping/palpation of the tibialis anterior/peroneal muscles and absent auditory feedback from light stroking of skin on the dorsal foot/lower shank (indicative of fibres directed towards the skin). These criteria have been shown previously to be indicative of microelectrode proximity to efferent post-ganglionic muscle sympathetic nerves[68]. All continuous data were digitized and stored using LabChart (Version 8; PowerLab; AD Instruments, NSW, Australia) at a sampling frequency of 1,000 Hz except for the MSNA signal, which was sampled at 10 kHz.

After acquiring a stable recording site, a 3 min baseline commenced followed by progressive ramp stimulation of the epidural stimulator device. The stimulation was increased by 0.5 V every 30-60 s. Multi-unit MSNA data were analyzed using a custom semi-automated LabView software program (National Instruments, Austin, TX)[65]. Muscle sympathetic action potential spikes were identified as waveforms that matched a triphasic morphology with the main phase being negative[66]. The negative deflections were only assessed if they were < -0.45 V, as a threshold outside the baseline noise width across all stimulation conditions. In the case of spontaneous multi-unit bursts becoming visible in the multi-unit (mean voltage) neurogram during the stimulation, we would identify the bursts only if rising above 3 times the noise width. To investigate whether the multi-unit bursts were gated from a supraspinal influence arising from the arterial baroreceptors, we quantified the burst latency as the difference between preceding candidate ECG R spikes. Latencies had to fall within a 1.0 to 1.6 second range for the possibility for arterial

baroreflex gating. We found that the mean burst latency was outside the normal range, at 0.774s (0.597s-0.982s) on average.

Amplitude mapping and implementation of closed loop procedures
We found a linear relationship between stimulation amplitudes (i.e., 0 to 7.5 mV) and pressor responses (see **Extended Data Figure 10**). During the closed-loop implementation, we monitored the patient's hemodynamic parameters using the finger plethysmography device described previously (See *Hemodynamic monitoring*). Baseline values were obtained in the supine position for approximately 5 mins. The patient was tilted upright up to a maximum of 70 degrees to induce orthostatic challenge. Using a feature selection algorithm, we extracted the mean blood pressure throughout the procedure. From the extracted mean blood pressure, we programmed a continuous stimulation output based on -(delta blood pressure)*beta (-Δ*β), where delta blood pressure is the change in blood pressure from baseline to upright tilt, and beta is the proportional coefficient. Using clinically-approved devices stimulation intensity was scaled every ~2s based on the calculated stimulation output in real-time. We performed two cycles of stimulation on and stimulation off which lasted approximately 5 mins for each condition during tilted upright position. We then quantified the target error values (See *Closed loop control of hemodynamics*) comparing the change in hemodynamics (i.e., systolic blood pressure, mean arterial pressure and diastolic blood pressure) for both conditions.   Stimulation was delivered using the N'VISION 8840 clinical controller.

Data analysis of spatial configurations
During an orthostatic challenge (See **Orthostatic challenge using a clinical tilt test**), changes in blood pressure were recorded in response to different spatial electrode configurations. We tested two sets of multipolar configurations. The first set includes three multipolar configurations along the rostro-caudal axis (i.e., rostral, middle and caudal spatial configurations), identified using a genetic algorithm, as we have previously described[12,21]. The second set is a comparison of the optimal rostro-caudal spatial configuration (i.e., posterior root stimulation) versus when the electrodes are switched between anodes and cathodes (i.e., posterior column stimulation). Blood pressure values were extracted from when the stimulation is off and during maximum stimulation amplitude for each spatial configuration (see **Extended Data Figure 10**). All blood pressure mean values and data points have been reported to compare stimulation off and stimulation on conditions for each spatial electrode configuration.

Questionnaires

The patient was asked three questions to compare experienced clinical burden before using EES and after using EES in their daily routine. The questions are as follows: 1) "On a scale of 0 to 10, can you rate how orthostatic hypotension affected your quality of life?", 2) How much dosage of midodrine do you take in a day (i.e., milligrams per day), and 3) "How often do you use compression garments in a week (i.e., days per week)?".

45. Ramsey, J. B. G. *et al.* Care of rats with complete high-thoracic spinal cord injury. *J. Neurotrauma* **27,** 1709–1722 (2010).

46. Anderson, M. A. *et al.* Required growth facilitators propel axon regeneration across complete spinal cord injury. *Nature* **561,** 396–400 (2018).

47. Squair, J. W. *et al.* High Thoracic Contusion Model for the Investigation of Cardiovascular Function after Spinal Cord Injury. *J. Neurotrauma* neu.2016.4518 (2016).

48. Asboth, L. *et al.* Cortico-reticulo-spinal circuit reorganization enables functional recovery after severe spinal cord contusion. *Nat. Neurosci.* **21,** 576–588 (2018).

49. Scheff, S. W., Rabchevsky, A. G., Fugaccia, I., Main, J. A. & Lumpp, J. E. Experimental modeling of spinal cord injury: characterization of a force-defined injury device. *J. Neurotrauma* **20,** 179–193 (2003).

50. van den Brand, R. *et al.* Restoring voluntary control of locomotion after paralyzing spinal cord injury. *Science* **336,** 1182–1185 (2012).

51. Krassioukov, A. V. & Weaver, L. C. Connections between the pontine reticular formation and rostral ventrolateral medulla. *Am. J. Physiol.* **265,** H1386-92 (1993).

52. Ueno, M., Ueno-Nakamura, Y., Niehaus, J., Popovich, P. G. & Yoshida, Y. Silencing spinal interneurons inhibits immune suppressive autonomic reflexes caused by spinal cord injury. *Nat. Neurosci.* **19,** 784–787 (2016).

53. Sundt, D., Gamper, N. & Jaffe, D. B. Spike propagation through the dorsal root ganglia in an unmyelinated sensory neuron: a modeling study. *J. Neurophysiol.* **114,** 3140–3153 (2015).

54. McIntyre, C. C. & Grill, W. M. Extracellular stimulation of central neurons: influence of stimulus waveform and frequency on neuronal output. *J. Neurophysiol.* **88,** 1592–1604 (2002).

55. Pan, C. *et al.* Shrinkage-mediated imaging of entire organs and organisms using uDISCO. *Nat. Methods* **13,** 859–867 (2016).

56. Lee, E. *et al.* ACT-PRESTO: Rapid and consistent tissue clearing and labeling method for 3-dimensional (3D) imaging. *Sci. Rep.* **6,** 18631 (2016).

57. Bria, A. & Iannello, G. TeraStitcher - a tool for fast automatic 3D-stitching of teravoxel-sized microscopy images. *BMC Bioinformatics* **13,** 316 (2012).

58. Rizk, A. *et al.* Segmentation and quantification of subcellular structures in fluorescence microscopy images using Squassh. *Nat. Protoc.* **9,** 586–596 (2014).

59. Kirshblum, S. C. *et al.* International standards for neurological classification of spinal cord injury (revised 2011). *J Spinal Cord Med* **34,** 535–546 (2011).

60. Bogert, L. W. J. & van Lieshout, J. J. Non-invasive pulsatile arterial pressure and stroke volume changes from the human finger. *Exp. Physiol.* **90,** 437–446 (2005).

61. Jansen, J. R. *et al.* A comparison of cardiac output derived from the arterial pressure wave against thermodilution in cardiac surgery patients. *Br. J. Anaesth.* **87,** 212–222 (2001).

62. Westerhof, B. E., Gisolf, J., Stok, W. J., Wesseling, K. H. & Karemaker, J. M. Time-domain cross-correlation baroreflex sensitivity: performance on the EUROBAVAR

data set. *J. Hypertens.* **22,** 1371–1380 (2004).

63. Wieling, W., Ganzeboom, K. S. & Saul, J. P. Reflex syncope in children and adolescents. *Heart* **90,** 1094–1100 (2004).

64. Whinnett, Z. I. *et al.* Multicenter randomized controlled crossover trial comparing hemodynamic optimization against echocardiographic optimization of av and VV delay of cardiac resynchronization therapy: the BRAVO trial. *JACC Cardiovasc. Imaging* **12,** 1407–1416 (2019).

65. Notay, K. *et al.* Validity and reliability of measuring resting muscle sympathetic nerve activity using short sampling durations in healthy humans. *J. Appl. Physiol.* **121,** 1065–1073 (2016).

66. Incognito, A. V. *et al.* Evidence for differential control of muscle sympathetic single units during mild sympathoexcitation in young, healthy humans. *Am. J. Physiol. Heart Circ. Physiol.* **316,** H13–H23 (2019).

67. Wallin, B. G. *et al.* Sympathetic single axonal discharge after spinal cord injury in humans: activity at rest and after bladder stimulation. *Spinal Cord* **52,** 434–438 (2014).

68. Incognito, A. V. *et al.* Pharmacological assessment of the arterial baroreflex in a young healthy obese male with extremely low baseline muscle sympathetic nerve activity. *Clin Auton Res* **28,** 593–595 (2018).